RESEARCH ARTICLE

Key Points:
- Sediment fluxes and budgets in the lower Seine Estuary are quantified under contrasted hydro- and meteorological conditions
- Wind/waves, tides, and river discharge impact sediment fluxes at specific locations along the estuary
- Seaward sediment export is enhanced during storm events and reduced during wet years

Correspondence to:
E. Schulz,
e.schulz.fischer@gmail.com

Suspended Sediment Dynamics in the Macrotidal Seine Estuary (France): 2. Numerical Modeling of Sediment Fluxes and Budgets Under Typical Hydrological and Meteorological Conditions

E. Schulz[1,2] , F. Grasso[1] , P. Le Hir[1], R. Verney[1], and B. Thouvenin[1]

[1]IFREMER – DYNECO/DHYSED, Centre de Bretagne, Plouzané, France, [2]Department of Physical Oceanography and Instrumentation, Leibniz Institute for Baltic Sea Research Warnemünde (IOW), Rostock, Germany

Abstract Understanding the sediment dynamics in an estuary is important for its morphodynamic and ecological assessment as well as, in case of an anthropogenically controlled system, for its maintenance. However, the quantification of sediment fluxes and budgets is extremely difficult from in-situ data and requires thoroughly validated numerical models. In the study presented here, sediment fluxes and budgets in the lower Seine Estuary were quantified and investigated from seasonal to annual time scales with respect to realistic hydro- and meteorological conditions. A realistic three-dimensional process-based hydro- and sediment-dynamic model was used to quantify mud and sand fluxes through characteristic estuarine cross-sections. In addition to a reference experiment with typical forcing, three experiments were carried out and analyzed, each differing from the reference experiment in either river discharge or wind and waves so that the effects of these forcings could be separated. Hydro- and meteorological conditions affect the sediment fluxes and budgets in different ways and at different locations. Single storm events induce strong erosion in the lower estuary and can have a significant effect on the sediment fluxes offshore of the Seine Estuary mouth, with the flux direction depending on the wind direction. Spring tides cause significant up-estuary fluxes at the mouth. A high river discharge drives barotropic down-estuary fluxes at the upper cross-sections, but baroclinic up-estuary fluxes at the mouth and offshore so that the lower estuary gains sediment during wet years. This behavior is likely to be observed worldwide in estuaries affected by density gradients and turbidity maximum dynamics.

1. Introduction

1.1. Estuarine Sediment Dynamics

Sediment fluxes and budgets are vitally important for the state of coastal and estuarine environments. They control water turbidity, surficial sediment nature, and morphological evolution so that they affect biochemical processes, ecological habitats, and human interests such as navigation issues. Due to different physical properties, e.g., settling velocities, and ecological relevance of gravel, sand, and mud, it is necessary to distinguish these sediment classes when investigating fluxes and budgets.

Sediment dynamics in an estuary are governed by various hydrodynamic, hydrological, meteorological, and sedimentary processes. The sediment of riverine and/or oceanic origin is (re)suspended by current and wave-induced bed shear stress and then transported and often accumulated in an estuarine turbidity maximum (ETM) by river discharge, residual circulation as well as tidal currents and asymmetries (e.g., Festa & Hansen, 1978; Geyer, 1993). Please be referred to the introduction of Part 1: Grasso et al. (2018) for a more detailed description of ETM formation.

Residual, i.e., temporally averaged sediment transport due to tidal asymmetries is referred to as tidal sediment pumping and can arise from (i) an asymmetric tidal wave, leading to a shorter flood phase with stronger currents and bed shear stress, compared to the ebb phase, as well as to a longer-lasting high-water (HW) slack, compared to low-water (LW) slack, and/or (ii) asymmetric tidal mixing related to tidal straining, leading to stronger stratification and vertical current shear during ebb, compared to flood (Allen et al., 1980; Burchard & Baumert, 1998; Burchard et al., 2013; Scully & Friedrichs, 2007). Cause (i) results in higher erosion

rates and thus higher sediment concentrations during flood as well as in higher deposition rates during HW slack (due to both the higher concentrations during flood and the longer-lasting HW slack promoting settling), i.e., a residual up-estuary transport (Brenon & Le Hir, 1999; Uncles et al., 1992). Cause (ii) results in reduced vertical mixing and thus surface-enhanced currents and lower sediment concentrations in the upper layer during ebb, compared to vertically uniform or bottom-enhanced currents and higher sediment concentrations in the upper layer during flood, i.e., also a residual up-estuary transport (Jay & Musiak, 1994).

Assuming periodic flow and negligible water depth variation, the total residual sediment flux at a given location, $\langle u\,c \rangle(x, y, z)$, can be split into two contributions:

$$\langle u\,c \rangle = \langle u \rangle \langle c \rangle + \langle u'c' \rangle \tag{1}$$

where u is the velocity, c is the sediment concentration, $\langle u \rangle = \int_T u\,dt\,/\,T$ is the residual velocity over the period T, and $u' = u - \langle u \rangle$ is the velocity fluctuation ($\langle c \rangle$ and c' analogue). $\langle u \rangle \langle c \rangle$ is called advective or transport flux; $\langle u'c' \rangle$, the covariance of u and c, is called (tidal) pumping or fluctuation flux (Burchard et al., 2013; Scully & Friedrichs, 2007; Sommerfield & Wong, 2011). After consultation with W. R. Geyer et al. (written communication, August 2016), we call $\langle u \rangle \langle c \rangle$ mean-flow flux and $\langle u'c' \rangle$ correlation flux. The latter term comprises the tidal asymmetries explained above (though cause (ii) contributes also to $\langle u \rangle$) as well as other fluctuations over T, e.g., of river discharge or wind.

The residual velocity, $\langle u \rangle$, comprises contributions from river discharge, gravitational circulation, tidal straining (cause (ii)), and laterally differential longitudinal advection, among other processes (Burchard et al., 2011; Jay & Musiak, 1994; Lerczak & Geyer, 2004). It thus depends on various parameters. For example, a higher river discharge, which implies a larger along-estuary salinity gradient, increases the gravitational (Festa & Hansen, 1976; Hansen & Rattray, 1965), the advectively driven, and the tidal straining circulation (Schulz et al., 2015), i.e., it increases $\langle u \rangle$ and thus the mean-flow sediment flux, $\langle u \rangle \langle c \rangle$.

1.2. Investigation of Sediment Fluxes and Budgets

While numerous studies have focused on the investigation of ETM (e.g., Allen et al., 1980; Cancino & Neves, 1999; Garel et al., 2009; Geyer, 1993; Jalón-Rojas et al., 2016; Le Hir et al., 2001; Yu et al., 2014) or mudflat dynamics (e.g., Deloffre et al., 2007; Talke & Stacey, 2008) and their forcing, studies focusing on the quantification and analysis of seasonal to annual sediment fluxes and budgets in estuaries are relatively rare. Applied methods range from

1. seismic profiles and geochemical analyses of sediment cores to quantify accumulation rates (Nitsche et al., 2010) over
2. point and profile measurements of velocities and sediment concentrations to quantify horizontal fluxes (French et al., 2008; Garel et al., 2009; Lindsay et al., 1996; McSweeney et al., 2016; Perez et al., 2000; Sommerfield & Wong, 2011; Uncles et al., 1985), sometimes combined with
   2.1. a box model (Yarbro et al., 1983) or
   2.2. a two-dimensional numerical model (Lambrechts et al., 2010), to
3. two- or three-dimensional numerical models of different complexity (regarding grid type, resolution, forcing, coupling with sediment and/or wave model, number of sediment classes etc.; Bi & Toorman, 2015; Bolle et al., 2010; Gleizon et al., 2003; Lumborg, 2005; Lumborg & Pejrup, 2005; Lumborg & Windelin, 2003; Ralston et al., 2012).

Some of these methods implicate problems limiting their applicability. The main problem with results based solely on measurements is the difficulty or even impossibility to extrapolate the observational data to an entire cross-section (Lindsay et al., 1996) and, in case of relatively short measurement series, to extrapolate it to longer periods (Perez et al., 2000). The main problem with two-dimensional models is the parameterization or even neglect of relevant vertically resolvable processes (e.g., gravitational circulation, in 2DH models; Bolle et al., 2010; Lumborg & Pejrup, 2005; Lumborg & Windelin, 2003) or transverse processes (e.g., transverse circulation, in 2DV along-estuary models; Gleizon et al., 2003).

The present study is based on a thoroughly calibrated and validated high-resolution three-dimensional hydrodynamic model coupled to a sediment model and forced by realistic boundary conditions including waves from a wave model (see section 2). The objective is to investigate the influence of different hydrological and meteorological conditions on estuarine sediment dynamics. Part 1 (Grasso et al., 2018) describes

the formation, location, and mass change of the ETM as well as the model validation; Part 2 (manuscript at hand) focuses on sediment fluxes and budgets on seasonal to annual time scales. To the authors' knowledge, such a detailed investigation has not been done before, neither with measurements (due to the problems mentioned above) nor with a comparably complex model. (A recent similar modeling study of sediment transport in the Scheldt estuary (Bi & Toorman, 2015, Figure 43 ff.) focused on the performance of different model implementations rather than on the influence of hydro- and meteorological conditions.)

1.3. Application to the Macrotidal Seine Estuary

The Seine Estuary is located in the northwestern part of France and stretches from the Bay of the Seine, open to the English Channel, to Poses (P in Figure 2a), where a weir limits the tidal influence. It is characterized by semidiurnal tides with a distinct fortnightly signal (spring-neap tidal range ratio of about 2; Figures 3b and 3c) and a tidal range reaching 8 m at Le Havre (LH in Figure 2b). In the estuarine parameter space spanned by freshwater Froude number and mixing number (Geyer & MacCready, 2014, Figure 6), the macrotidal Seine Estuary ranges between the Chesapeake Bay (strongly stratified) and the James River (partially mixed) at the estuary mouth as well as between the Hudson River (strongly stratified) and the Conwy River (strain-induced periodic stratification, SIPS) at Honfleur (Hon in Figure 2b), depending on the river discharge and the tidal phase with respect to the fortnightly cycle.

With a catchment area of more than 79,000 km^2, the Seine is one of the largest rivers on the northwestern European continental shelf. The discharge (Q) amounts to 440 m^3/s on average (at Poses, 1941–2014), but can fall below 100 m^3/s in a dry summer and exceed 2,000 m^3/s in a rain-laden winter (Figure 1m). The dominant wind direction is southwest with average wind speeds of about 4 m/s (Figures 1a–1d) and peaks of more than 15 m/s, particularly from November to January (Figure 1b). Waves enter the bay from northwest with typical significant wave heights of 0.5 m and peaks of more than 3.5 m in front of the estuary mouth (results from wave model, section 2.1). The funnel-shaped estuary is exposed to the prevailing westerly winds and waves so that the intertidal regions at the mouth are subject to erosion under the combined effect of waves and currents (Deloffre et al., 2007; Verney et al., 2007).

The lower estuary is characterized by the presence of a distinct estuarine turbidity maximum (ETM; Avoine et al., 1981), which exerts a pronounced control on the sedimentation patterns of subtidal areas and intertidal mudflats from the estuary mouth to upstream of Tancarville (Tan in Figure 2b) (Brenon & Le Hir, 1998; Deloffre et al., 2007). Grasso et al. (2018, Part 1, section 4) observed that the ETM location is strongly modulated by the semidiurnal tides with increased excursion during spring tides. The tidally averaged ETM location is mainly related to the Seine river discharge, lying around Fatouville (Fat in Figure 2b) for average Q, shifted downstream close to the western end of the dykes (DN and DS) for high Q and shifted upstream close to Tancarville for low Q. The ETM mass reaches approximately 0.5×10^9 kg during spring tides, but is not notably affected by the river discharge. Nevertheless, wave events can significantly increase the ETM mass, particularly during periods of high river discharge, i.e., when the ETM is located near the wave-induced sediment resuspension on the banks at the estuary mouth.

During the last two centuries, the Seine Estuary has been vastly altered by human activity (Avoine et al., 1981). As a result, the lower estuary has been transformed from a dominantly natural system to an anthropogenically controlled system, with dykes (built to enhance the ebb currents in the channel, to reduce maintenance dredging) as well as continuous dredging of the navigational channels and dumping of the dredged sediment close to the estuary mouth. Considering these ongoing interventions, quantifying and understanding sediment fluxes and budgets in the Seine Estuary is of great importance. The present study focuses on the influence of typical and extreme hydro- and meteorological conditions.

2. Methods: Numerical Model, Setup, and Postprocessing

A three-dimensional numerical model has been developed to study the hydro- and sediment dynamics of the Seine Estuary from the Bay of the Seine to the weir at Poses (Figure 2a) with a particular interest on the lower estuary from the mouth to Tancarville (Figure 2b), corresponding to the main area of the ETM excursion. Part 1 (Grasso et al., 2018, sections 2.2 and 3) of this paper provides a detailed description of the numerical model setup and the validation of hydro- and sediment dynamics. The main model characteristics are repeated in sections 2.1 and 2.2.
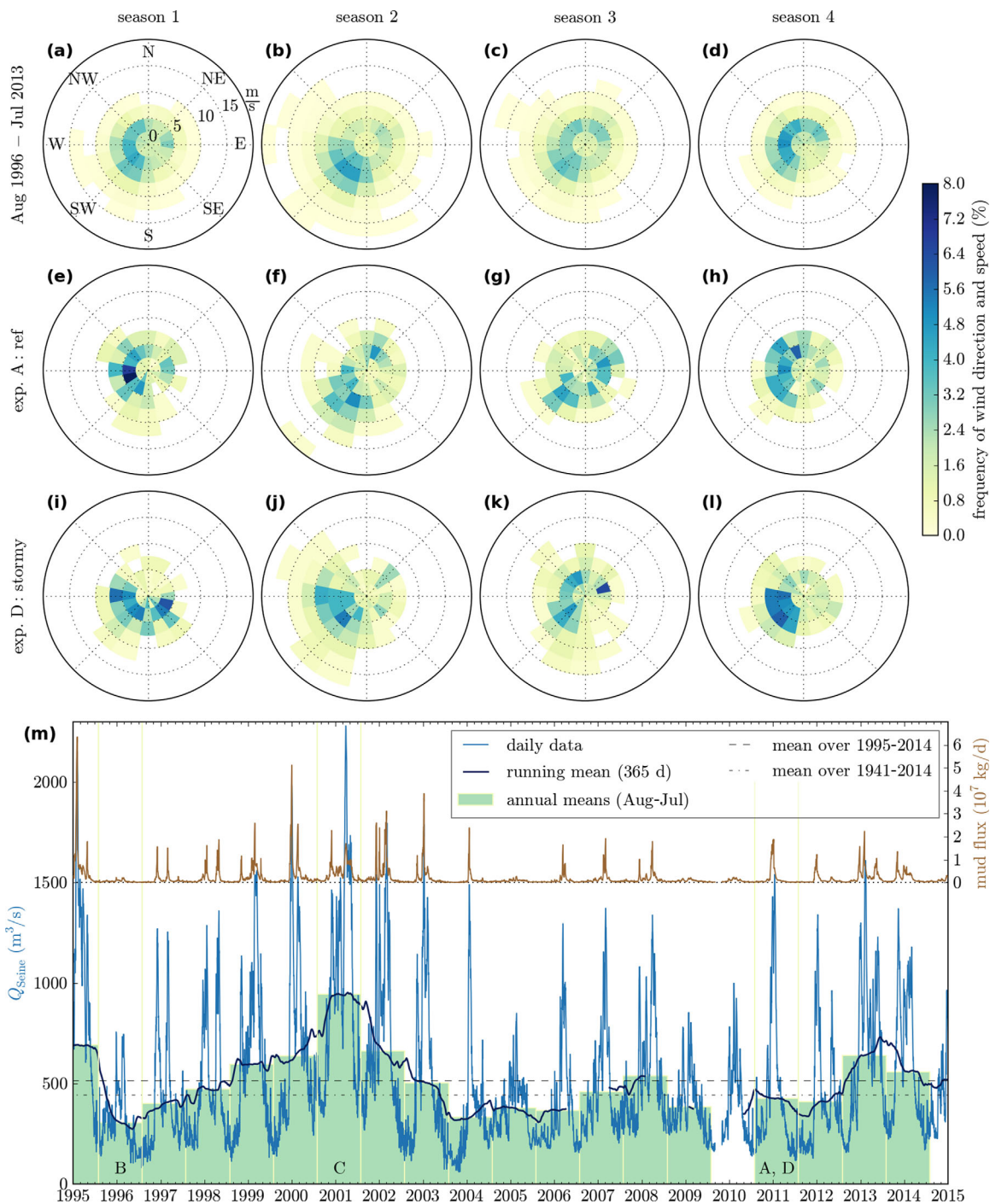
Figure 1. (a–l) Windroses presenting the frequency of occurrence of wind directions (wind origins, 16 bins) and wind speeds (8 bins, size 2.5 m/s) split into four seasons (columns) of different periods (rows; source: ARPEGE model, Meteo-France). For the long-term windroses (covering 17 years, first row), the seasons are (a) August–October, (b) November–January, (c) February–April, and (d) May–July; for the experiment-wise windroses (second and third row), the seasons are as defined in section 2.3. (m) Daily and mean river discharge as well as daily mud flux at Poses over 20 years (source: Groupement d'intérêt public Seine-Aval, public interest group lower Seine). The letters A–D indicate the source periods of the river data applied in the model experiments (section 2.3, Table 2, Figure 3).

It should be noted that sediment fluxes and budgets cannot be directly validated due to lack of comparable data (also see section 3.5). The hydrodynamic model provides good skills, as presented in Part 1 (Grasso et al., 2018, sections 3.1–3.3), and most of the simulation errors arise from modeling the complex suspended sediment dynamics. The error margin of the simulated sediment concentration is found in Part 1 (section 3.5,
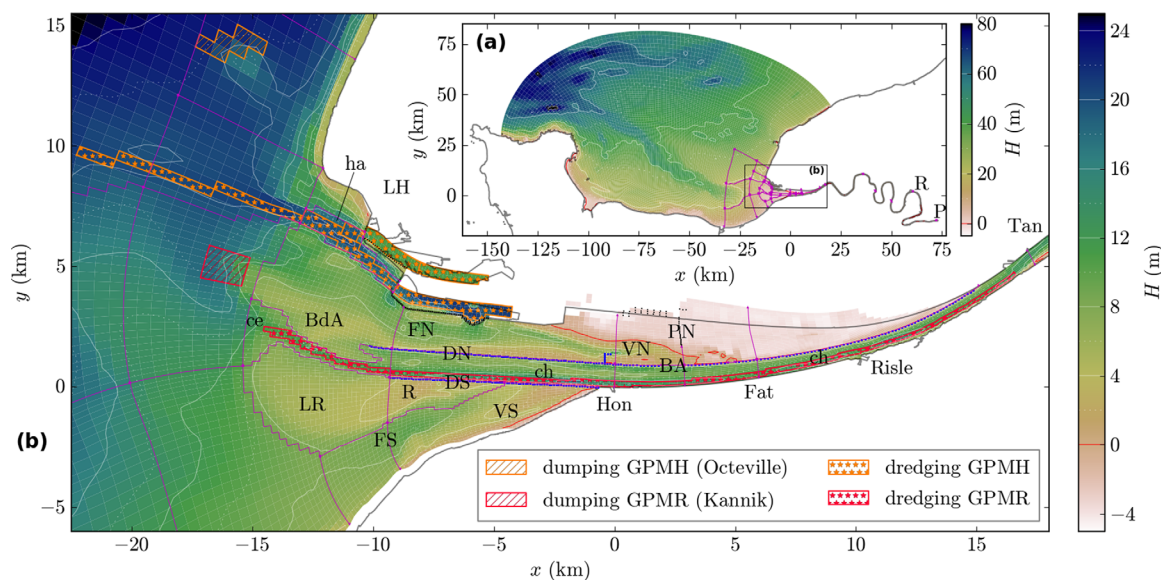
Figure 2. Bathymetry of (a) entire model domain (longitude 1.75°W to 1.24°E, latitude 49.29°N to 50.16°N) and (b) region of interest. Blue dotted lines mark submerged dykes; magenta lines mark borders for the calculation of fluxes and budgets; hachures mark dredging and dumping sites (legend; GPMH, Grand Port Maritime du Havre; GPMR, Grand Port Maritime de Rouen). Town abbreviations in plot a: R, Rouen; P, Poses; in plot b: LH, Le Havre; Hon, Honfleur; Fat, Fatouville; Tan, Tancarville. Further abbreviations in plot b: ha, harbor access; ce, Engainement, channel entrance; ch, channel; BdA, Banc d'Amfard; LR, Les Ratelets; R, Ratier; FN/FS, Fosse Nord/Sud, northern/southern fosse; DN/DS, Digue Basse Nord/Sud, northern/southern submerged dyke; VN/VS, Vasière Nord/Sud, northern/southern mudflat; BA, Brèche Aval, breach downstream of PN; PN, Pont de Normandie, bridge of Normandy.

Figure 7) to be 23–34% for 81–95% of the time and maximum 63–65% for high-concentration events (11% of the time). However, the error margin has to be put in perspective to the fact that in-situ measurements at pier-base monitoring stations are likely to overestimate the sediment concentration in the channel due to local phenomena (Part 1, section 2.3). Altogether, the quantification of the Seine Estuary SPM dynamics is expected to be associated with an error margin lower than 50% at tide-averaged time scales. Such skills, based on 1-year high-frequency measurements carried out at three locations, provide a satisfactory level of confidence to investigate the suspended sediment dynamics in a macrotidal estuary from tidal to annual time scales (e.g., Amoudry et al., 2014; Bi & Toorman, 2015; Toublanc et al., 2016; Yu et al., 2014).

2.1. Hydrodynamic Model

The hydrodynamic model applied in this study is the hydrostatic model MARS3D (Model for Applications at Regional Scale, Lazure & Dumas, 2008). A nonorthogonal curvilinear grid was chosen to better respect the estuarine shape (details in Kervella et al., 2012), to optimize the computational costs by lengthening the grid cells in the direction of dominant tidal flows and to improve sediment flux calculations. Cell sizes ranged from about $30 \times 100 \, \text{m}^2$ at the estuary mouth to $2 \times 2 \, \text{km}^2$ in the English Channel. The water column was discretized by 10 equidistant σ (sigma) layers. The adaptive time step ranged from 2 to 18 s.

The hydrodynamic model was forced by the main tidal components from the CST France database (SHOM) at the sea boundary as well as by wind stresses and pressure gradients provided by the meteorological ARPEGE model (Meteo-France). Waves were simulated by means of the WAVEWATCH III® (WW3) model (Ardhuin & Roland, 2012) on a series of embedded computational grids, from a large-scale model of the Atlantic Ocean down to a local model with the same resolution as the hydrodynamic model. It allows to compute the total bed shear stress (τ_b) as a combination of current-induced ($\tau_{b,c}$) and wave-induced ($\tau_{b,w}$) bed shear stresses. The realistic Seine river discharge and mud supply (measured/estimated at Poses, see Part 1: Grasso et al., 2018, end of section 2.2.2) as well as a constant Risle river discharge ($15 \, \text{m}^3/\text{s}$) were taken into account. Further details regarding the forcing can be found in section 2.3.

2.2. Sediment Model

The hydrodynamic model was coupled with a process-based sediment model for sand and mud mixtures (Le Hir et al., 2011). The sediment bed was discretized by up to 100 layers of variable thickness ranging

Table 1
Sediment Parameters and Their Values[a]

Parameter	Symbol	Value
Grain diameter	d_{gravel}	$5{,}000\,\mu m$
	$d_{sand,coarse}$	$800\,\mu m$
	$d_{sand,medium}$	$210\,\mu m$
	$d_{sand,fine}$	$100\,\mu m$
	d_{mud}	$20\,\mu m$
Settling of mud, equation (2)		
Minimum settling velocity	$w_{s,min}$	$0.1\,mm/s$
Maximum settling velocity	$w_{s,max}$	$1.5\,mm/s$
		exp. E: $1.0\,mm/s$
Calibration parameters	a	0.30
	b	0.18
	c_1	$3.0\,mm/s$
	c_2	0.79
Deposit concentrations, equation (8)		
Gravel/sand concentration	$C^*_{gravel/sand}$	$1{,}600\,kg/m^3$
Mud concentration	C^*_{mud}	$625\,kg/m^3$

[a]"exp. E" refers to a model experiment with lower $w_{s,max}$ (section 3.4).

from 10^{-3} to 5 mm. This multilayer model accounts for the vertical and temporal variations of sand and mud content in the bed as well as for segregation and consolidation processes. In the water column, the model solves the 3-D advection-diffusion equation (3) for different classes of particles. In this study, five classes of sediment (one gravel, three sands, and one mud; diameters in Table 1), representative of the Seine Estuary sediment modes, were initially distributed over a 1 m thick bed according to the measured sediment distribution (Lesourd et al., 2016).

The gravel was defined as a sand class, which was considered as a two-dimensional variable with constant settling velocity depending on the grain diameter and computed following Soulsby (1997, equation (102)). The mud class was considered as a three-dimensional variable with a varying settling velocity ($w_{s,mud}$) according to van Leussen (1994):

$$w_{s,mud} = \max\left[w_{s,min}, \min\left(w_{s,max}, c_1\, C^{c_2}_{mud}\, \frac{1+a\,G}{1+b\,G^2} \right) \right], \qquad (2)$$

where C_{mud} is the mud concentration (kg/m^3), G is the turbulent shear rate (1/s), and a, b, c_1, c_2 are calibration parameters (Table 1). This dependence on mud concentration and turbulence is aimed at representing flocculation processes. The mud settling velocity was minimized ($w_{s,min}$) and maximized ($w_{s,max}$) according to in-situ measurements carried out in the Seine Estuary in the framework of the FLUMES project (Seine-Aval 4 research program).

The erosion flux is based on Partheniades-Ariathurai's formulation (Partheniades, 1965) and depends on the mass fraction of mud in order to distinguish cohesive and noncohesive sediment behaviors. Consolidation is simulated by solving Gibson's equation for mixed sediments (Gibson et al., 1967), taking into account segregation processes (during the settling), permeability, and effective stress regimes of the sedimentation/consolidation phases (Grasso et al., 2015). For further details as well as the calibration and validation of the model, please be referred to Part 1 (Grasso et al., 2018, sections 2.2.2–3).

The maintenance of the harbors Le Havre (Grand Port Maritime du Havre, GPMH) and Rouen (Grand Port Maritime de Rouen, GPMR) as well as their access channels (Figure 2b) requires extensive sediment dredging and dumping activities in the lower estuary (Marmin et al., 2014). Since these anthropogenic fluxes are of the same order of magnitude as the quasinatural sediment fluxes (see table and figures in sections 3.1–3.3), dredging and dumping need to be taken into account to properly simulate sediment dynamics in the Seine Estuary. Here, the sediment model simulated these activities by removing the upper sediment layers in the dredged areas every 10 min if the sediment deposit exceeded a given elevation corresponding to the minimum water depth provided by the GPMH and GPMR. The dredged sediment mass was then released in the lowest cell of the water columns in the associated dumping areas, i.e., Octeville for the GPMH and Kannik for the GPMR (Figure 2b). The dredging and dumping areas in the model correspond to the actual sites. It should be noted that the model could well reproduce measured dredged masses (see Part 1: Grasso et al., 2018, end of section 3.4).

Morphodynamic coupling was not applied in this study. It should be noted that simulations including morphodynamic coupling were carried out for comparison and yielded negligible changes after 1 year.

For the calculation of sediment fluxes and budgets, we defined more than 50 borders and 30 zones (Figure 2). The computation was performed directly in MARS3D in order to cumulate the fluxes at every time step to ensure sediment mass conservation. Output was quarter-hourly. Details are given in section 2.4.

2.3. Model Forcing Experiments, Spin-Up, and Evaluation Periods

In order to investigate the effect of different hydro- and meteorological conditions on sediment fluxes and budgets, four model experiments with different realistic forcings were carried out. An overview is given in Table 2 and the forcing itself is shown in Figure 3. This approach allowed to assess interannual variability between dry and wet years as well as between calm and stormy years while the effects of the different types of forcing could be separated. Different combinations of forcings, on the other hand, are characteristic of different times of the year (see list of seasons below) and investigated with regard to their joined effect.

Table 2
Overview of Model Experiments, Applied Forcings, and Their Source Periods[a]

Experiment	River discharge (m³/s)	Wind, waves, tides
A Reference	Typical (433), 2010–2011	Calm, 2010–2011
B Low Q	Low (309), 1995–1996	Calm, 2010–2011
C High Q	High (958), 2000–2001	Calm, 2010–2011
D Stormy	Typical (433), 2010–2011	Stormy, 2011–2012

[a]The average river discharge over one lunar year (see end of section 2.3) is stated in parentheses.

Seasonal fluctuations of the sediment dynamics between dry and calm summer and wet and stormy winter months were explored on the basis of a reference year (2010–2011) with typical river discharge (Q; typical in terms of annual average and seasonality, see section 1.3 and Figure 1m) and relatively calm wind (experiment A, all forcing from 2010–2011; Table 2, Figures 3a and 3b). The influence of the river discharge on annual and seasonal sediment fluxes and budgets was assessed by means of replacing only Q with that of a dry year (exp. B, Q from 1995–1996) or a wet year (exp. C, Q from 2000–2001; date-conform shift of Q; keeping wind, waves, and tides from 2010–2011; Table 2, Figures 3a and 3b). To investigate the impact of strong wind events and an extremely stormy winter (2011–2012, Figure 3c), we simulated the stormy year with its meteorological conditions and its tides (thus accounting for the influence of tidal elevation on wave height) and again replaced only Q (exp. D; keeping wind, waves and tides from 2011–2012; replacing Q with that of the reference year, 2010–2011; Table 2, Figures 3a and 3c). For comparability, the combination of river discharge and tides was kept the same as in experiment A (Figure 3).

A spin-up period of 1 year, 1 August 2010 to 1 August 2011, with forcing according to experiment A preceded each simulation evaluated in this study. In order to obtain results free from artificial effects of the transition, particularly the jump in the river discharge at the start of experiment C, evaluation began only on 31 July 2010 (exps. A–C) and on 19 August 2011 (exp. D), indicated by the first dashed purple line in Figure 3.

In order to exclude tidal variations (semidiurnal as well as fortnightly) from the long-term analyses of fluxes and budgets so as to ensure comparability of results obtained over different periods, e.g., seasons (with typical river discharge and wind/wave conditions), we defined the following evaluation periods based on lunar months (synodic cycles of the Moon, 29.5306 days):

1. season: 88.5 days (three lunar months, 171 M_2 cycles)
   (a) season 1 (summer-autumn; low Q, calm-moderate):
       31 July 2010 20:00 to 28 October 2010 08:00 (exps. A–C),
       19 August 2011 20:00 to 16 November 2011 08:00 (exp. D)
   (b) season 2 (autumn-winter; high Q, stormy):
       28 October 2010 08:00 to 24 January 2011 20:00 (exps. A–C),
       16 November 2011 08:00 to 12 February 2012 20:00 (exp. D)
   (c) season 3 (winter-spring; medium-high Q, moderate):
       24 January 2011 20:00 to 23 April 2011 08:00 (exps. A–C),
       12 February 2012 20:00 to 11 May 2012 08:00 (exp. D)
   (d) season 4 (spring-summer; low Q, calm):
       23 April 2011 08:00 to 20 July 2011 20:00 (exps. A–C),
       11 May 2012 08:00 to 7 August 2012 20:00 (exp. D)
2. lunar year: 354 days (four seasons, 12 lunar months)

The seasons are indicated in Figure 3. "Annual" fluxes and budgets refer to fluxes and budgets evaluated over one lunar year. All evaluation periods start and end at low water (LW).

2.4. Computation of Sediment Fluxes and Budgets
The transport equation solved in MARS3D reads

$$0 = \frac{\partial DC_i}{\partial t} + \frac{\partial D\left(uC_i - k_x \frac{\partial C_i}{\partial x}\right)}{\partial x} + \frac{\partial D\left(vC_i - k_y \frac{\partial C_i}{\partial y}\right)}{\partial y} + \frac{\partial D\left(w^* C_i - \frac{k_z}{D^2}\frac{\partial C_i}{\partial \sigma}\right)}{\partial \sigma} ,$$ (3)

where $D = H + \eta$ is the water depth (H is the bathymetry, η is the surface elevation), C_i is the concentration of sediment class i (in the water), t is the time, x and y are the horizontal coordinates, $\sigma = (z - \eta)/D$ is the vertical coordinate (z is the geopotential coordinate), u and v are the horizontal velocities, w^* is the vertical velocity in σ coordinates, k_x and k_y are the horizontal eddy diffusivity coefficients, and k_z is the vertical eddy diffusivity (Lazure & Dumas, 2008).
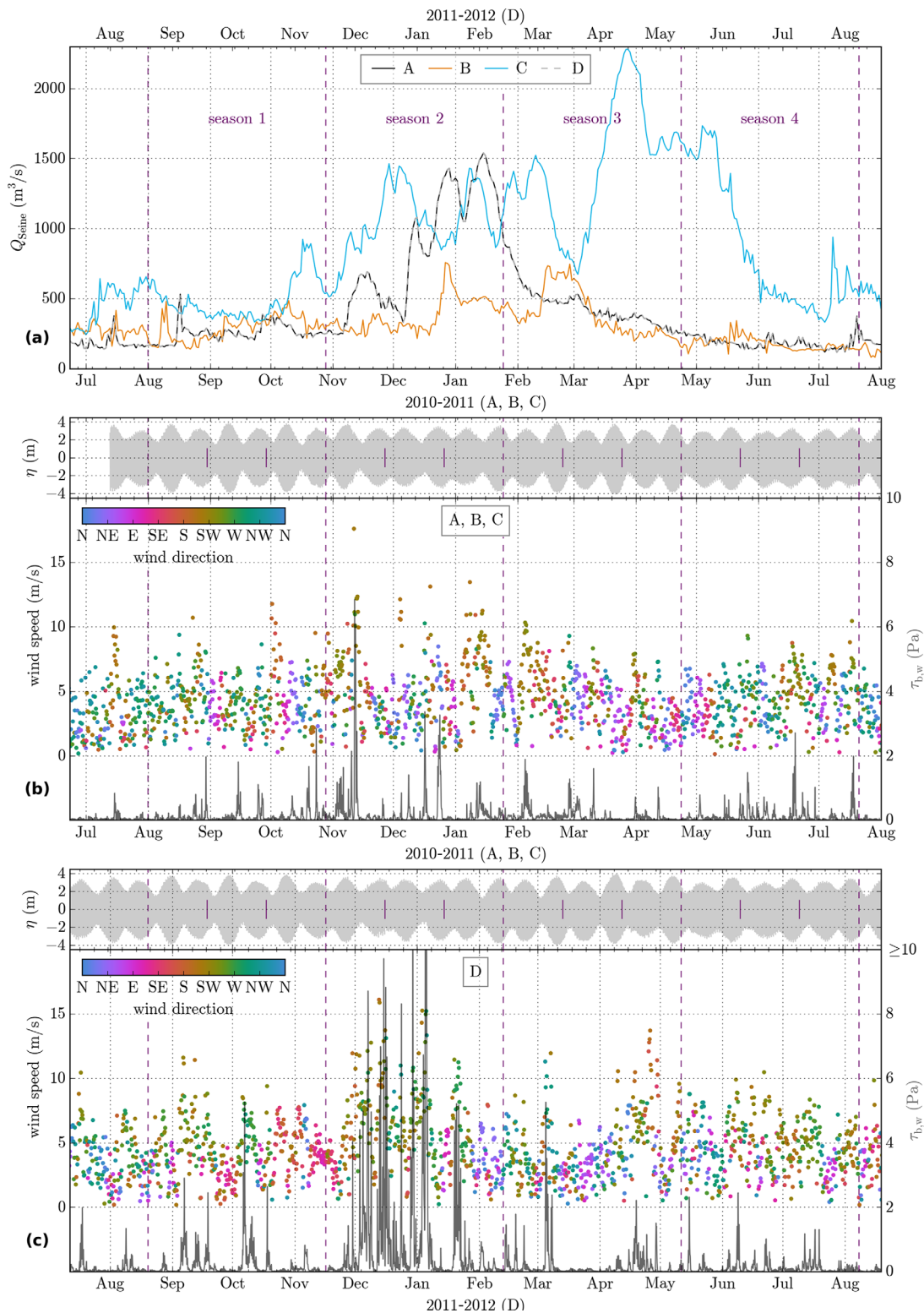
Figure 3. Overview of applied forcing: (a) river discharge at Poses (P in Figure 2a) in experiments A–C (lower) and D (upper time axis); (b) tidal elevation (model result) at Honfleur (Hon in Figure 2b), wind speed and direction, as well as wave-induced bottom shear stress in front of the estuary mouth (wave model result) in experiments A–C; (c) same as plot b, but in experiment D. Dashed purple lines mark seasonal evaluation periods; short solid purple lines in η mark lunar months (29.5 days); minor time ticks mark weeks (Sundays).

The horizontal advection-diffusion terms were used to calculate the cumulative mass flow (e.g., of chemical contaminants, Thouvenin et al., 2007) through a border, which is composed of adjoined cell interfaces in the $y - z$ plane (length L_y) and/or the $x - z$ plane (length L_x) (C-grid; Arakawa & Lamb, 1977):

$$m_{\mathcal{F},i}(t) = \int_0^t \left[\int_{L_y} \int_{-H}^{\eta} \left(uC_i - k_x \frac{\partial C_i}{\partial x} \right) dz\, dy + \int_{L_x} \int_{-H}^{\eta} \left(vC_i - k_y \frac{\partial C_i}{\partial y} \right) dz\, dx \right] d\tilde{t} . \tag{4}$$

The mass of sediment class i contained in a zone, i.e., the area A enclosed by borders (and shorelines), is composed of the deposited and the suspended mass:

$$m_{\mathcal{B},i}(t) = \int_A \left[\int_{-\delta_s}^{0} \tilde{C}_i(x, y, z_s, t)\, dz_s + \int_{-H}^{\eta} C_i(x, y, z, t)\, dz \right] d\tilde{A} , \tag{5}$$

where $\tilde{C}_i$ is the concentration of sediment class i in the bed, δ_s is the thickness of the sediment bed, and z_s is the vertical coordinate in the sediment bed. (The vertical position $z_s = 0$ corresponds to $z = -H$.) The contribution of dredging and dumping is included in $m_{\mathcal{B},i}$ (also see section 2.2 and end of this section). It should be noted that the suspended mass (second summand) is much smaller than the deposited mass (first summand) and included only for the sake of completeness.

For sediment class i, residual fluxes ($\mathcal{F}_i$, kg/d), i.e., temporally averaged mass flow rates per border, and budgets ($\mathcal{B}_i$, kg/d), i.e., residual mass change rates per zone, were then defined as

$$\mathcal{F}_i(t_1, t_2) = \frac{m_{\mathcal{F},i}(t_2) - m_{\mathcal{F},i}(t_1)}{t_2 - t_1} \quad \text{and} \tag{6}$$

$$\mathcal{B}_i(t_1, t_2) = \frac{m_{\mathcal{B},i}(t_2) - m_{\mathcal{B},i}(t_1)}{t_2 - t_1} . \tag{7}$$

The instants t_1 and t_2 coincide with low water (LW) in order to avoid sensitivity effects at highly dynamic tidal phases such as full flood and because of possible multiple HW peaks in the specific case of the Seine Estuary (often two HW due to tidal resonance in the eastern English Channel; Le Hir et al., 2001; Le Provost et al., 1986).

To improve the comparability between differently large zones, sediment mass budgets ($\mathcal{B}_i$, kg/d) were transformed to sediment thickness budgets ($\mathcal{T}_i$, mm/d; zone colors in Figures 4 and 5) by division by deposit concentration (C_i^*, Table 1) and zone area (A),

$$\mathcal{T}_i = \frac{\mathcal{B}_i}{C_i^* A} . \tag{8}$$

It should be noted that C_i^* (Table 1) represents typical deposit concentrations, as opposed to (lower) concentrations of fresh deposits or (higher) concentrations of old, consolidated sediment.

The dredged and dumped masses of sediment class i ($m_{\mathcal{D},i}$; negative/positive for dredging/dumping) were cumulated per budget zone in MARS3D. Analogue to the budgets (7), residual dredging/dumping rates ($\mathcal{D}_i$, kg/d) were calculated from $m_{\mathcal{D},i}$. For the transformation from mass to thickness, the zone area was applied analogue to (8) (rather than the dredging/dumping site area). This allows the visual assessment of the contribution of dredging and dumping to the budgets (comparison of triangle and zone colors in Figures 4 and 5).

3. Results and Discussion: Sediment Fluxes and Budgets Under Different Forcing

The simulations' results are visualized by means of spatial maps of residual sediment fluxes and budgets per experiment (and lunar year, Figure 4) and per season (for reference experiment, Figure 5) as well as by means of time series of cumulative sediment flow, ordered by experiment (to compare cross-sections and relate to forcing, Figure 6) and ordered by cross-section (to compare experiments, Figure 7). Focus is on the total sediment (sum of all five classes, see section 2.2; hereafter referred to as "sediment") and on the mud fraction.
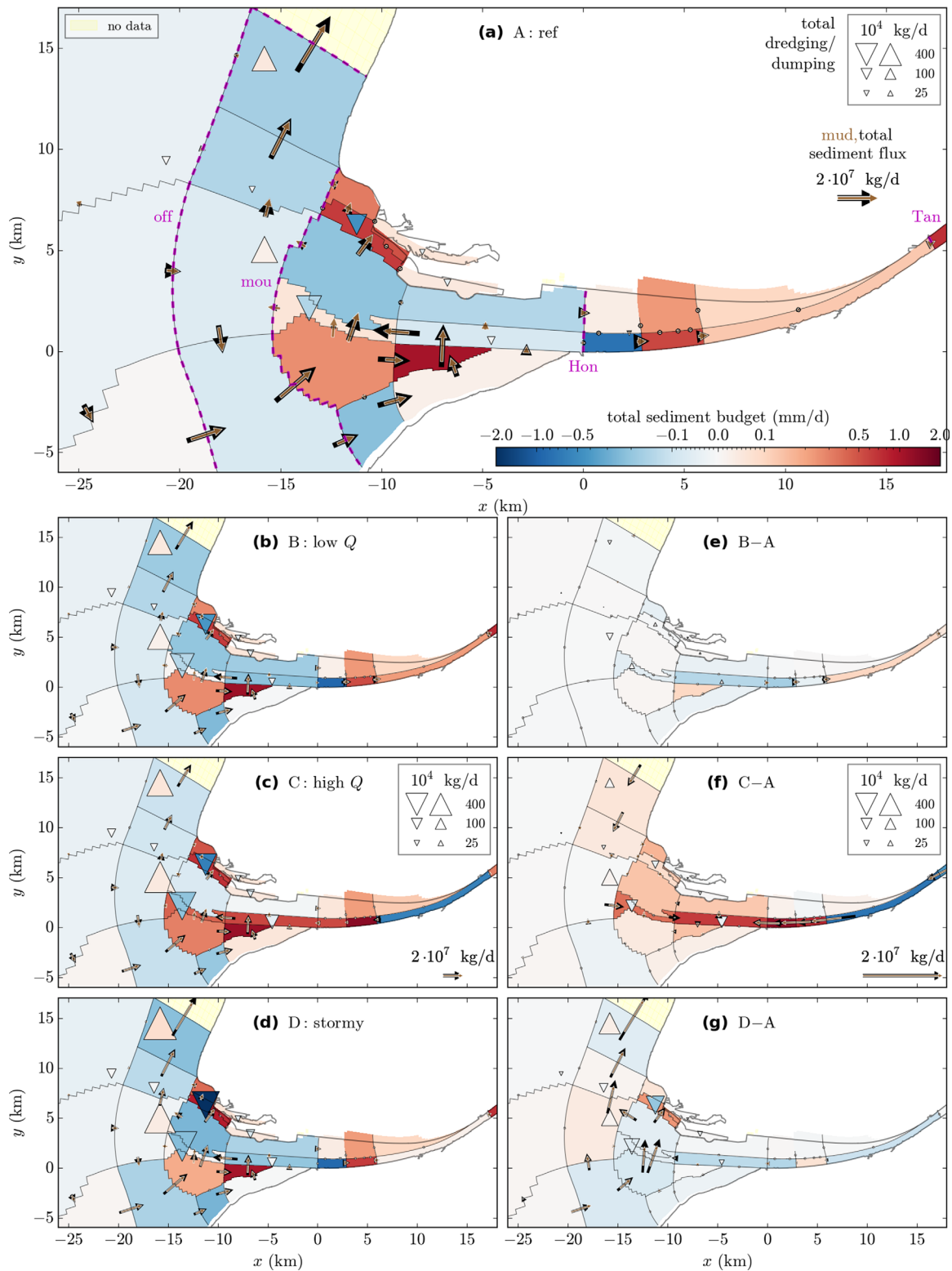
Figure 4. Residual sediment fluxes (arrows: mud in brown, total in black), total sediment budgets (colors: loss in blue, gain in red; semi-logarithmic scale), dredging (upside-down triangles), and dumping (upright triangles) in the lower estuary and in front of the estuary mouth in experiments A–D (plots a–d) over one lunar year (354 days). Plots e–g show the differences of experiments B–D to the reference experiment, A. Dashed magenta lines in plot a mark cross-sections for the mass flow shown in Table 3 and Figures 6–8.
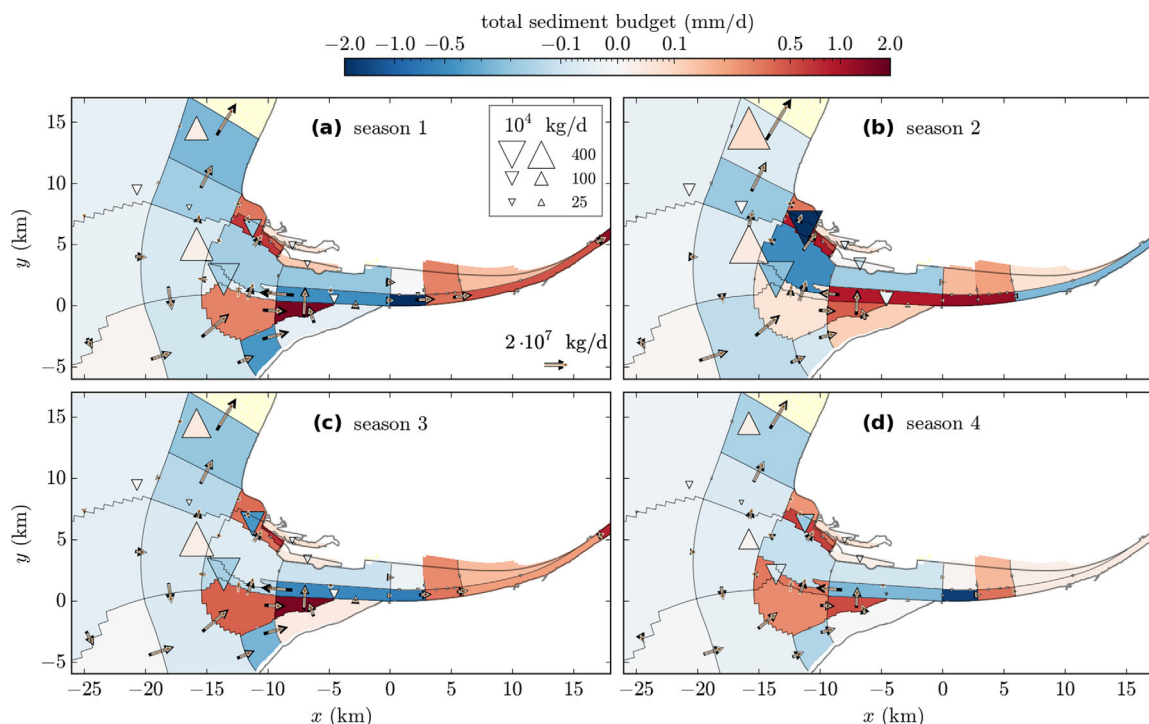
Figure 5. Same as Figure 4, but in experiment A only and in four seasons (plots).

3.1. Flux and Budget Patterns in the Reference Experiment (A)
3.1.1. Annual Scale

Figure 4a represents residual sediment fluxes and budgets in experiment A over one lunar year, hereafter referred to as "annual." The fluxes (arrows; mud in brown, total sediment in black) exhibit a counterclockwise eddy around the southern part of the estuary mouth. Sediment is transported eastward, toward, and into the estuary along the southern coast and then flushed northward over the southern submerged dyke (DS in Figure 2b). It leaves the estuary westward through the channel (ch, ce) as well as north- and westward over the Banc d'Amfard (BdA) and via the harbor access (ha) of Le Havre before it is transported northward away from the estuary. This pattern is related to the direction of the tidal wave propagating eastward through the English Channel and to the predominantly southwest wind direction (section 1.3, Figures 1e–1h).

Comparison of the mud (brown) and the total sediment fluxes (black arrows; Figure 4a) reveals that the mud fraction is responsible for more than 50%, in some places for more than 90%. The coarser fractions (gravel and sands, difference of black and brown arrows) exhibit considerably weaker spatial dynamics.

The annual mass flow through four cross-sections (each from shore to shore) is given in Table 3 (exp. A, period year). The mass flow is directed up-estuary through the cross-sections at the estuary mouth, Honfleur, and Tancarville (columns mou, Hon, Tan) and down-estuary, i.e., seaward, at the offshore cross-section (off).

Channel, harbors, and harbor access are subject to dredging (blue, upside-down triangles in Figure 4a; together -377×10^7 kg; Table 3, columns GPMH and GPMR). Still, due to deposition on areas which are not dredged, the harbor access gains 61×10^7 kg sediment (light red color), 87% of which is mud. Deposition also dominates on the southern banks, i.e., Les Ratelets and Ratier (LR and R in Figure 2b), as well as upstream of the bridge of Normandy (PN). The other zones lose sediment (light blue), particularly the channel between Honfleur (Hon) and the bridge.

3.1.2. Seasonal Scale

Figure 5 represents sediment fluxes and budgets in experiment A over season 1 to season 4. While seasons 1, 3, and 4 exhibit patterns similar to each other and to the lunar year (Figure 4a, described in section 3.1.1), season 2 (Figure 5b) stands out.

Between Tancarville and Fatouville (Tan and Fat in Figure 2b), the channel loses sediment (without being dredged) instead of gaining it whereas between the bridge of Normandy and the western end of the
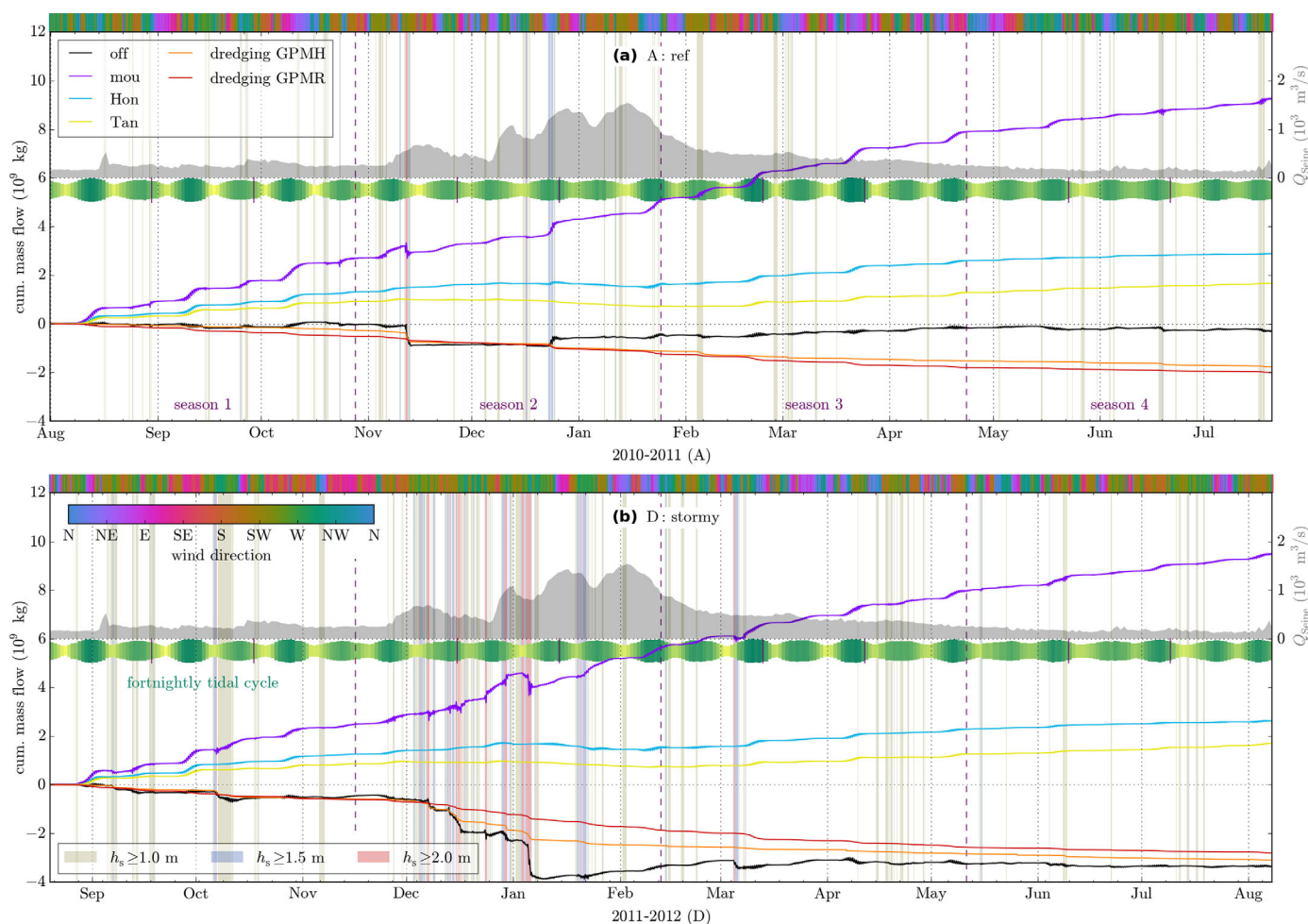
Figure 6. Cumulative total sediment flow (positive up-estuary) through four cross-sections (legend in plot a, left column; offshore, estuary mouth, Honfleur, Tancarville; indicated in Figure 4a) as well as dredging (negative) at two sites (GPMH, GPMR; marked in Figure 2b) in experiments A and D (plots). Also shown are river discharge (grey-filled curves), spring and neap tides (green and yellow), wind direction (multicolor horizontal bars), and periods of high waves (beige, blue, and pink vertical bars; legends in plot b). Dashed purple lines mark seasonal evaluation periods; short solid purple lines mark lunar months (29.5 days); minor time ticks mark weeks (Sundays).

dykes, the channel gains sediment instead of losing it (Figure 5b). This shift of sediment mass is probably related to a down-estuary displacement of the estuarine turbidity maximum (ETM) due to the relatively high river discharge in season 2 (Figure 3a) (Cancino & Neves, 1999; Garel et al., 2009; Grasso et al., 2018, Part 1).

It should be noted that the mass flow through the cross-section at Honfleur is still directed up-estuary, but it is much smaller than during seasons 1 and 3 and accounts for only 11% of the annual mass flow (8% for mud fraction; Table 3, exp. A, period season 2 versus year, column Hon). The mass flow through the cross-section at Tancarville, on the other hand, is directed down-estuary only in season 2 (column Tan), again due to the relatively high river discharge in this period (also see section 3.1.3).

Along with season 2, also season 4 exhibits a comparably small up-estuary mass flow through the cross-section at Honfleur (Table 3). This seems to be related to the smaller spring-tide amplitudes in this period (Figures 3b and 6a): As described in section 3.1.3, the up-estuary mass flow is particularly large during the higher spring tides. A strong sensitivity of sediment fluxes to the tidal range was also observed by Lindsay et al. (1996). It should be noted that the spring-tide amplitudes are smaller also in season 2 (semiannual tidal cycle), but the influence of river discharge and storms appears to dominate in that period.

In the region between the offshore cross-section and the western end of the dykes, the northward fluxes are larger in season 2 than in the other three seasons, particularly the flux into the harbor access of Le Havre
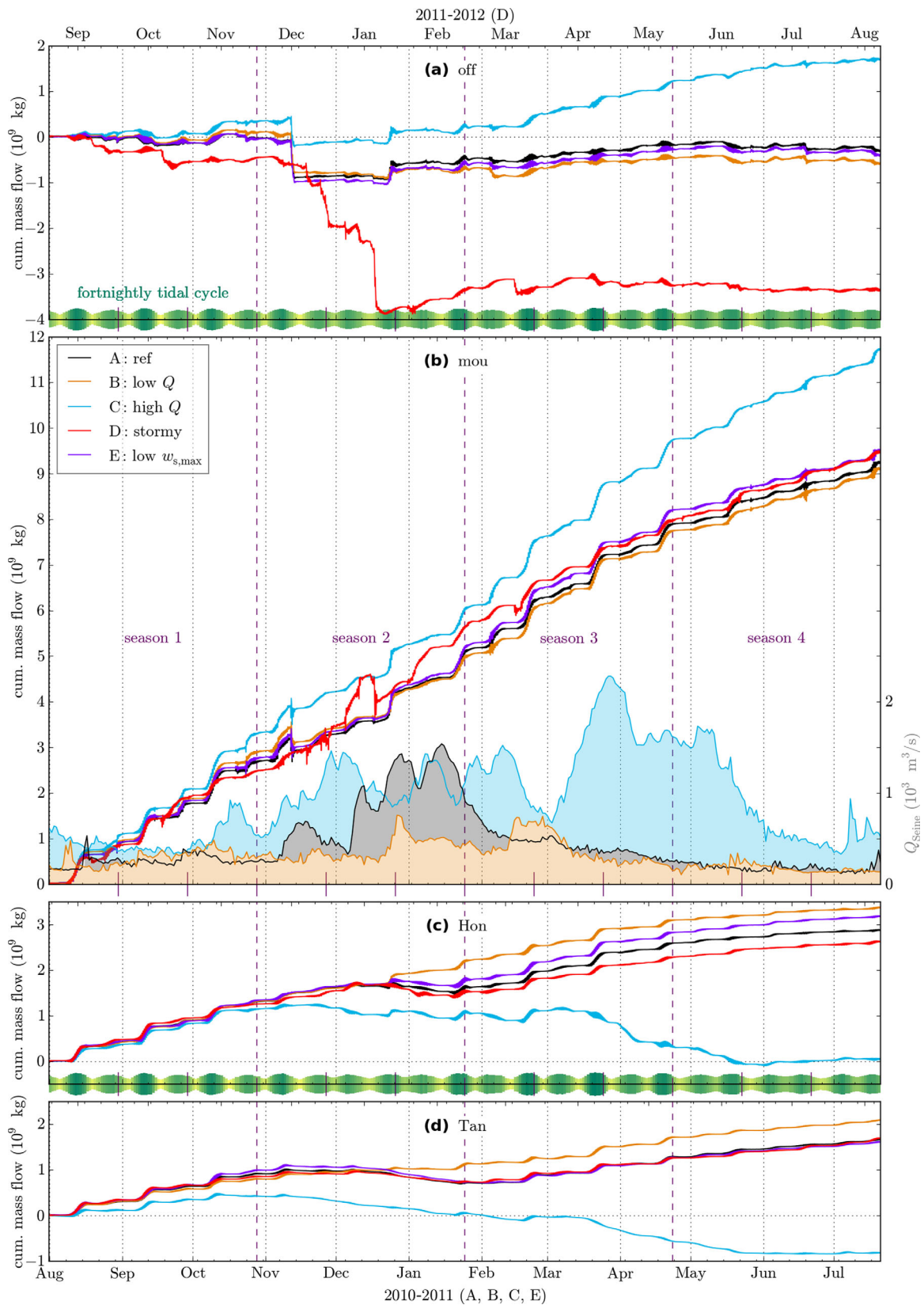
Figure 7. Cumulative total sediment flow (positive up-estuary) through four cross-sections (plots; offshore, estuary mouth, Honfleur, Tancarville; indicated in Figure 4a) in experiments A–E (legend in plot b). Also shown are river discharge (filled curves in plot b) and spring and neap tides (green and yellow). Dashed purple lines mark seasonal evaluation periods; short solid purple lines mark lunar months (29.5 days); minor time ticks mark weeks (Sundays).

Table 3
Cumulative Mass Flow and Dredging of Total Sediment (Black Numbers) and Mud Fraction (Brown Numbers) in Experiments A–E and in Five Evaluation Periods[a]

| Exp. | Period | Cum. mass flow (10^7 kg) through cross-section | | | | | | | | Dredging (10^7 kg) at site | | | |
		off		mou		Hon		Tan		GPMH		GPMR	
A	Year	−32	6	924	373	287	178	166	131	−177	−126	−200	−36
A	Season 1	−5	5	267	97	130	79	91	73	−27	−22	−52	−9
A	Season 2	−43	−31	237	98	31	14	−20	−20	−85	−54	−72	−14
A	Season 3	29	25	284	114	98	59	57	45	−41	−31	−56	−8
A	Season 4	−13	7	136	65	29	26	38	33	−24	−20	−20	−5
B	Year	−60	−6	910	359	337	221	209	165	−173	−123	−186	−30
B	Season 1	8	14	288	110	131	79	80	64	−27	−21	−55	−10
B	Season 2	−80	−51	205	75	87	60	32	24	−82	−51	−62	−9
B	Season 3	24	23	280	110	91	57	60	45	−39	−31	−50	−7
B	Season 4	−13	8	137	64	28	25	38	33	−25	−20	−19	−4
C	Year	170	138	1,172	552	4	−37	−82	−87	−203	−144	−278	−86
C	Season 1	32	30	329	132	114	66	42	32	−27	−21	−69	−15
C	Season 2	−11	−9	269	121	−7	−14	−38	−37	−99	−64	−83	−20
C	Season 3	100	70	375	181	−75	−70	−61	−59	−47	−36	−78	−29
C	Season 4	49	48	200	118	−27	−19	−26	−23	−30	−23	−48	−23
D	Year	−336	−116	947	384	262	155	169	130	−309	−189	−280	−51
D	Season 1	−46	−32	247	83	125	72	85	69	−59	−42	−61	−9
D	Season 2	−293	−116	313	147	26	6	−11	−14	−191	−102	−126	−29
D	Season 3	12	27	234	92	77	47	52	38	−34	−27	−71	−9
D	Season 4	−9	4	153	62	35	30	43	38	−25	−18	−23	−4
E	Year	−42	−3	950	391	318	203	161	130	−187	−132	−172	−29
E	Season 1	−6	3	274	101	133	81	99	79	−30	−24	−44	−7
E	Season 2	−54	−37	239	99	43	23	−26	−24	−90	−55	−64	−10
E	Season 3	31	29	305	128	106	69	54	43	−39	−28	−47	−8
E	Season 4	−13	2	132	64	36	29	35	33	−29	−24	−17	−4

[a]The evaluation period "year" refers to a lunar year, i.e., the sum of seasons 1–4. The mass flow is positive up-estuary; dredging implies a negative mass change. The four cross-sections (offshore, estuary mouth, Honfleur, Tancarville) are indicated in Figure 4a; the two dredging sites (GPMH, GPMR) are marked in Figure 2b. The data in experiments A–D, period one lunar year correspond to Figures 4a–4d (except mud dredging, not shown); the data in experiment A, seasons 1–4 correspond to Figure 5 (except mud dredging).

(Figures 5b versus 5a, 5c, 5d). The sediment gain on Les Ratelets (south of channel entrance) is smaller and the sediment loss on the Banc d'Amfard (north of channel entrance) is larger. The larger fluxes and the (relative) sediment loss south and north of the channel entrance are probably due to the stronger wind, particularly from southwest (Figure 1f), and higher waves in season 2 (Figures 3b and 6a), causing more erosion and thus higher suspended sediment concentrations as well as stronger wind-driven currents. The effect of individual storm events is discussed in section 3.1.3.

According to the larger northward fluxes, the sediment gain and thus the dredging in the harbor access are much larger in season 2. The dredging in the channel entrance is also larger, though at this location it may also be due to the down-estuary displacement of the ETM. Corresponding to the larger dredging, there is much more dumping in front of the estuary mouth. The dredging in season 2 accounts for 42% of the annual dredging (Table 3, columns GPMH and GPMR).

3.1.3. Shorter Time Scales

Figure 6a represents the evolution of the cumulative sediment mass flow through four cross-sections as well as the evolution of the cumulative dredged mass at the two dredging sites. The influence of river discharge, tides, wind, and waves (also in Figure 6a) changes along the estuary as described in this section. To support the results, correlations of mass flux (per cross-section) with different forcings are shown in Figure 8.
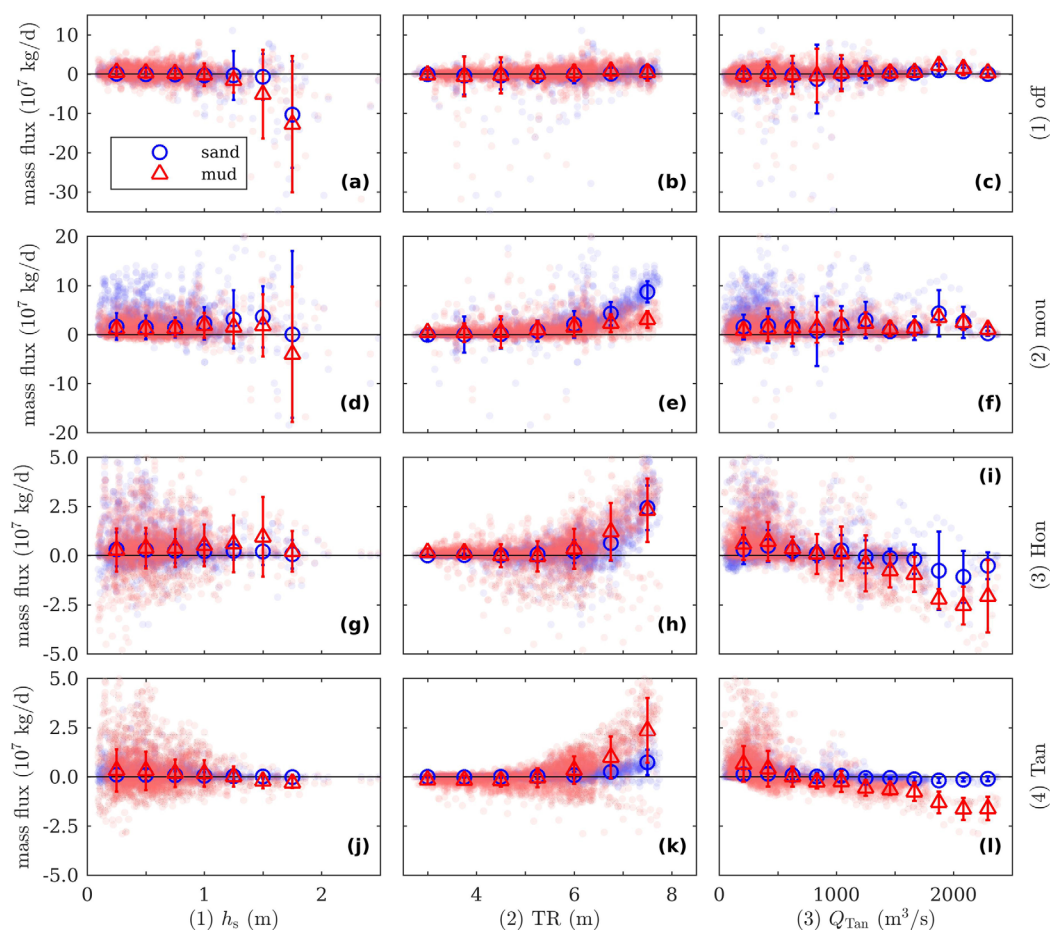
Figure 8. Sand (blue) and mud flux (red dots; positive up-estuary) averaged over 1 M_2 cycle correlated with forcing averaged over 4 M_2 cycles (3 previous plus current cycle) in experiments A–D. Circles/triangles and bars mark mean value and standard deviation per forcing bin, respectively. Rows (labeled on the right) correspond to cross-sections (offshore, estuary mouth, Honfleur, Tancarville; indicated in Figure 4a). Columns correspond to forcings: (1) significant wave height, (2) tidal range at Honfleur, and (3) river discharge at Tancarville.

The river discharge mainly affects the mass flux through the upper cross-sections, i.e., at Honfleur (Hon) and Tancarville (Tan; Figure 6a, also Figures 8i and 8l). A relatively high river discharge barotropically counteracts up-estuary and favors down-estuary fluxes (i.e., mass flow rates) and thus shifts the ETM down-estuary (Cancino & Neves, 1999; Garel et al., 2009; Part 1: Grasso et al., 2018); accordingly, the cumulative mass flow (positive up-estuary) is reduced, particularly in the third lunar month of season 2 (Figure 6a). At the lower cross-sections, i.e., at the estuary mouth (mou) and offshore (off), this effect is negligible compared to the influence of tides (Figure 8f versus 8e), wind, and waves (Figure 8c versus 8a; see below).

A fortnightly tidal signal is visible at all four cross-sections (Figure 6a). The cumulative mass flow exhibits larger temporal fluctuations during spring than during neap tides, implying that both the up-estuary (during flood) and the down-estuary (ebb) fluxes are larger during spring tides. This is related to stronger tidal currents and thus more erosion and higher suspended sediment concentration. At the higher spring tides, the mass flow through the estuary mouth exhibits a distinct positive step (Figure 6a, strong positive correlation of tidal amplitude and mass flux in Figure 8e), implying that the up-estuary flux is larger than the down-estuary flux (tidal pumping, see introduction; e.g., Le Hir et al., 2001). These steps are also visible at Honfleur and Tancarville, though they are smaller there (weaker correlation in Figures 8h and 8k) because uHL_y (4), and thus the fluxes are smaller in shallower and narrower cross-sections. The mass flow through the offshore cross-section also exhibits small steps at the higher spring tides, but their direction depends on the wind direction (next paragraph). While dredging at the offshore sites and the harbor access of Le Havre (GPMH) does not react to the tides (Figures 6a), dredging in the channel entrance and channel

(GPMR) also exhibits small steps at the higher spring tides (Figure 6a). This is related to the before-mentioned larger up-estuary mass flux through the mouth during spring tides due to tidal pumping (also see Part 1: Grasso et al., 2018, section 4).

Wind and waves do not influence the mass flux through the upper cross-sections (Hon, Tan; Figure 8h and 8j), but they can have a strong impact at the estuary mouth and particularly offshore (Figures 6a and 8a). While weak storms with wave heights between 1.0 and 1.5 m (beige vertical bars in Figure 6a) hardly have any effect, stronger storms with wave heights above 1.5 m (blue) or even 2.0 m (pink) cause significant up- or down-estuary residual fluxes in this region, depending on the wind direction: The storm event from west-southwest in the second week of November 2010 (highest wind speed, wave height, and wave-induced bottom shear stress in the lunar year, Figure 3b) leads to a significant seaward flux through the offshore cross-section, while the storm event from north-northeast in the fourth week of December 2010 leads to a considerable landward flux (Figure 6a). This behavior can also be observed at the estuary mouth, though the effect is smaller there and partly concealed by the strong fortnightly signal (see above). The down-estuary mass flux during the storm event in the second week of November 2010, coinciding with spring-neap transition, approximately compensates the up-estuary mass flux during a higher spring tide (see above). It should be noted that the seaward fluxes at the offshore cross-section which are larger than 10×10^7 kg/d (dots below -10×10^7 kg/d in Figure 8a) are always associated with winds from the quadrant south-southwest to west-northwest.

3.2. Effect of Lower or Higher River Discharge (Experiments B and C)

Figures 4b and 4c represent annual sediment fluxes and budgets in experiments B and C; Figures 4e and 4f represent their differences to the reference experiment, A. Experiment B (309 instead of 433 m^3/s average river discharge, Table 2) exhibits results very similar to experiment A. The differences B–A (also Table 3, exp. B versus A, period year) are a small reverse version of the differences C–A and therefore not discussed in detail.

Experiment C (958 instead of 433 m^3/s average Q, Table 2) exhibits large differences to experiment A. The annual flux and budget patterns in experiment C (Figure 4c) resemble the season 2 patterns in experiment A except for the large wind- and wave-driven sediment loss occurring there around the channel entrance (Figure 5b, described in section 3.1.2). The largest annual differences C–A are the sediment loss upstream and the sediment gain downstream of Fatouville, particularly in the channel (Figure 4f). This shift is associated with down-estuary fluxes in the channel from Honfleur to Tancarville (all up-estuary in exp. A; Figure 4c versus 4a) and related to a down-estuary displacement of the ETM due to the higher river discharge in experiment C (Figure 3a; cp. exp. A, season 2 in section 3.1.2) (Grasso et al., 2018, Figures 7a and 8a).

It should be noted that the annual mass flow through the cross-section at Honfleur (channel and northern mudflat) is still directed up-estuary, but it amounts to only 1% of that in experiment A (Table 3, exp. C versus A, period year, column Hon; Figure 7c). The mass flow through the cross-section at Tancarville, on the other hand, is directed down-estuary in experiment C (up-estuary in exp. A; Table 3, column Tan; Figure 7d), again due to the higher river discharge in this experiment (cp. exp. A, season 2).

At the estuary mouth and particularly at the offshore cross-section, the effect is reverse: A 27% larger amount of sediment (with respect to exp. A) is transported up-estuary through the mouth (Table 3, exp. C versus A, period year, column mou; Figure 7b) and more than the fivefold of what is transported seaward through the offshore cross-section in experiment A is transported landward in experiment C (Table 3, column off; Figure 7a). This seems to contradict the expected effect of a higher river discharge (smaller up-estuary/landward and larger down-estuary/seaward sediment mass flow, as at Honfleur and Tancarville), but it can be explained by estuarine circulation and the tidal pumping mechanism detailed hereafter (Dronkers, 1986; Dyer, 1973; Yu et al., 2014).

The higher river discharge in experiment C shifts the salt wedge downstream (Grasso et al., 2018, their Figures 7a and 8a) and thus implies larger horizontal salinity gradients (not shown) at these wider and deeper cross-sections. A larger along-estuary salinity gradient and a larger depth drive a stronger estuarine circulation (Burchard et al., 2011; Hansen & Rattray, 1965). Figure 9 represents the residual velocity (considering water depth variation, i.e., $\langle Du \rangle / \langle D \rangle$) through the border northeast of the dumping site Octeville and through the channel entrance (see Figure 2b) in experiments A and C. These borders are the parts of the offshore and the mouth cross-section, respectively, which are most affected by different Q (Figure 4f).
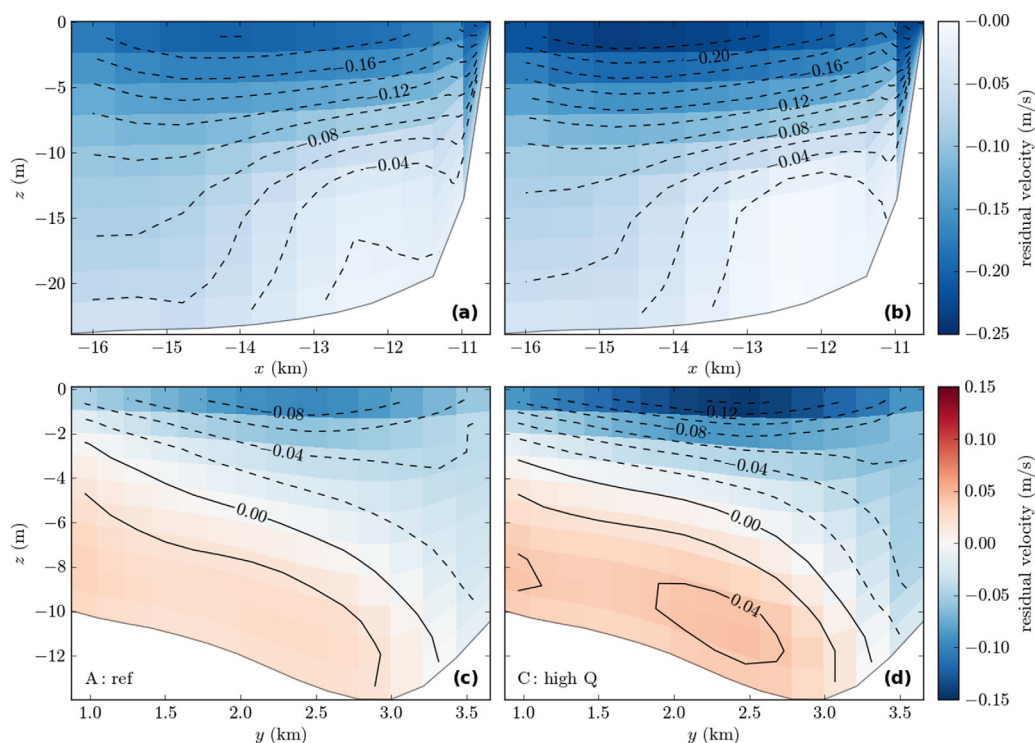
Figure 9. Residual velocity (averaged over one lunar year, positive up-estuary) through (a, b) the border northeast of the dumping site Octeville and (c, d) the channel entrance in (a, c) experiment A and (b, d) experiment C.

At the border northeast of the dumping site Octeville (northern part of offshore cross-section, off in Figure 4a), there is no residual inflow, but outflow extends over the entire water column. However, the vertical shear of the residual velocity is stronger in experiment C than in experiment A (Figure 9b versus 9a). The smaller outflow above the bottom in experiment C combined with lower residual sediment concentrations (not shown) causes less sediment outflow through the border (smaller mean-flow sediment flux, $\langle u \rangle \langle c \rangle$, see introduction), which leads to sediment inflow through the entire offshore cross-section since the sediment inflow through the western parts of the cross-section does not change (Figures 4f, 4c versus 4a). It should be noted that the correlation flux ($\langle u'c' \rangle$) through the northern border plays only a minor role for the mud fraction (largest fraction in terms of flux) and the total sediment. This indicates that tidal as well as intra-annual forcing fluctuations are not important for mud and total sediment fluxes offshore.

The estuarine circulation through the channel entrance (central part of mouth cross-section, mou in Figure 4a) is much stronger in experiment C than in experiment A; the outflow at the surface and the inflow above the bottom are larger (Figure 9d versus 9c). Due to stronger salinity stratification, also the vertical gradient of the residual sediment concentration is stronger in experiment C; the concentration at the surface is lower and the concentration at the bottom is higher in experiment C (not shown). Combined (mean-flow sediment flux, $\langle u \rangle \langle c \rangle$, see introduction), this favors sediment inflow through the border. However, further analysis of the residual sediment flux reveals that the correlation flux ($\langle u'c' \rangle$) is the dominant contribution at the channel entrance for all sediment fractions.

At the channel entrance and over one lunar year, the cumulative mass flow of mud is down-estuary (exp. A: -231×10^7 kg, exp. C: -136×10^7 kg) while the cumulative mass flow of fine and medium sand is up-estuary (exp. A: 115×10^7 kg, exp. C: 196×10^7 kg). The cumulative mass flow of coarse sand and gravel is up-estuary, too, but relatively small (exps. A, C: 1×10^7 kg). With respect to experiment A, the down-estuary mud flow is decreased and the up-estuary sand flow is increased in experiment C so that the total cumulative mass flow through the channel entrance is shifted from down-estuary in experiment A (-115×10^7 kg) to up-estuary in experiment C (61×10^7 kg). This leads to larger sediment inflow through the entire mouth cross-section since the flow through the southern and northern parts of the cross-section hardly changes (Figures 4f, 4c versus 4a).

The increased up-estuary sand flow in experiment C is likely caused by an increased tidal mixing asymmetry (cause (ii) in section 1.1) and the increased estuarine circulation, both related to the larger along-estuary salinity gradient (stronger tidal straining circulation; Schulz et al., 2015). This also explains the decrease of the down-estuary mud flow (i.e., relative shift toward up-estuary flow), but not the down-estuary direction itself.

In both experiments, the mud concentration at the channel entrance is highest at the end of ebb and at the southern slope (not shown), possibly related to mud flushed down from the bank Les Ratelets (LR in Figure 2b). This local phenomenon favors sediment outflow. Then, in experiment C, the strong salinity stratification at the end of ebb allows a strong velocity shear so that flood currents arise in the lower part of the cross-section while surface currents are still ebb-directed (not shown). It seems that also this early flood-directed flow reduces the sediment outflow (exp. C versus A), in addition to the increased tidal mixing asymmetry and estuarine circulation, but a more detailed analysis is beyond the scope of this study.

Furthermore, the dredging activities affect the mass flux through the estuary mouth. Sediment dredged upstream of the mouth cross-section is obviously no longer available for down-estuary fluxes through the cross-section, i.e., dredging acts as a sediment sink with regard to these fluxes. Dredging in the channel entrance and channel is increased by 39% (GPMR; 15% GPMH) in experiment C with respect to experiment A (Table 3, exp. C versus A, period year).

3.3. Effect of More Frequent and Stronger Storms (Experiment D)

Figure 4d represents annual sediment fluxes and budgets in experiment D; Figure 4g represents their differences to the reference experiment, A. Experiment D (stormier than exp. A, particularly in season 2; Figure 3c versus 3b, also Figures 1i–1l versus 1e–1h) exhibits annual flux and budget patterns similar to experiment A, i.e., fluxes in the same direction and sediment loss or gain occurring in the same zones (Figure 4d versus 4a), but the northward fluxes in the region between the offshore cross-section and the western end of the dykes are larger (Figure 4g). Accordingly, the sediment loss is larger and the sediment gain is smaller in this region except in the harbor access of Le Havre (ha in Figure 2b). Due to the wind coming predominantly from southwesterly directions (Figure 3c and 1i–1l), the harbor access (enclosed in the north and east) easily traps sediment. More frequent and stronger storms necessitate more dredging at that site (exp. D versus A: +75% for GPMH, +40% for GPMR; Table 3, period year), as already observed in the stormy season 2 in experiment A (section 3.1.2; cp. Figures 4d and 5b).

As explained in section 3.1.3, the influence of wind and waves is largest offshore and insignificant farther up-estuary (also see Figure 8). This is very evident when comparing the mass flow in experiments A and D (Table 3, Figure 7). While the seaward annual mass flow through the offshore cross-section is more than 10 times larger in experiment D, the mass flow through the three upper cross-sections differs by less than 10%.

However, the mass flow through the estuary mouth exhibits distinct responses to storms with wave heights above 2.0 m (pink vertical bars in Figure 6b). The flow direction during these events does not depend on the wind direction alone, but also on the river discharge and the tidal phase with respect to the fortnightly cycle. It should be noted that the phase with respect to the semidiurnal cycle can also impact the residual flow, particularly for wind events lasting only a few hours so that a tidal asymmetry can be created, enforced, or counteracted (Talke & Stacey, 2008), but these short time scales are beyond the scope of this study.

In conclusion, the seaward mass flow through the offshore cross-section in the stormy season 2 accounts for 87% of the annual mass flow (Table 3, exp. D, season 2 versus year, column off), which highlights the impact of stormy periods on the annual estuarine sediment dynamics.

3.4. Sensitivity of Sediment Fluxes to the Mud Settling Velocity

To estimate the sensitivity of the fluxes to the chosen sediment parameters, an additional experiment, E, is carried out, in which the maximum settling velocity of mud is reduced to $w_{s,max} = 1.0$ mm/s (instead of 1.5 mm/s; Table 1). The settling velocity of mud ($w_{s,mud}$) was observed to be close to its maximum value ($w_{s,max}$) most of the time so that reducing $w_{s,max}$ by 33% presents a significant constraint. However, both values lie in the common range for estuarine environments. $w_{s,mud}$ is one of the most critical parameters as it considerably affects the sediment concentrations (e.g., Lumborg & Windelin, 2003). A lower settling velocity enhances sediment suspension and thus, modifies ETM intensity and advection; $w_{s,mud}$ is therefore

commonly used as one of the main calibration parameters when modeling suspended sediment dynamics (Part 1: Grasso et al., 2018, sections 2.2.2–2.3). Here, the objective is to quantify the effect of a lower $w_{s,max}$ on the sediment fluxes. All other parameters and the forcing in experiment E are the same as in experiment A (Table 2; Figures 3a and 3b). The spin-up strategy is also the same (section 2.3), though with $w_{s,max} = 1.0$ mm/s already during the spin-up.

Comparison of the mass flow in experiments A and E yields only small differences (Table 3, Figure 7). With a lower maximum settling velocity of mud (exp. E), the mass flow of mud is more dynamic, i.e., mostly higher in both the up- and the down-estuary direction (brown numbers in Table 3). This is in agreement with higher concentrations of suspended mud, which can be expected when reducing the settling velocity. Accordingly, less mud is deposited and needs to be dredged in the channel entrance and the channel (GPMR). At the offshore and northeastern dredging sites (GPMH), on the other hand, more dredging of mud is required because more suspended mud is transported and eventually deposited there.

Changing the settling velocity of mud also affects the sand dynamics; comparing experiments A and E, the differences of the total sediment mass flow (black numbers) are mostly larger than the differences of the mud mass flow (Table 3). This can be explained by the influence of the relative mud fraction in the sea bed on the erosion of sand. As described in Part 1 (Grasso et al., 2018, section 2.2.2), a lower relative mud fraction (resulting from reduced settling) shifts the erosion flux of both sand and mud toward the erosion flux of pure sand, which is higher than that of pure mud (e.g., Le Hir et al., 2011). Thus, more sand can be eroded and transported (in total sediment mass flow in Table 3, exp. E versus A). Accordingly, less sand remains deposited and needs to be dredged in the channel entrance and the channel (GPMR). At the offshore and northeastern dredging sites (GPMH), on the other hand, analogue to the dredging of mud (end of previous paragraph), more dredging of sand is required because a higher relative mud fraction (resulting from more inflow) shifts the erosion flux of both sand and mud toward the lower erosion flux of pure mud.

Overall, comparison of the annual sediment mass flow with different $w_{s,max}$ (exp. E versus A) yields only minor differences (less than 11% except offshore, where the absolute mass flow is relatively small; Table 3, columns mou, Hon, Tan), which provides confidence to the robustness of numerical modeling of sediment fluxes and budgets from seasonal to annual time scales.

3.5. Representativeness of Sediment Flux Simulations

A quantification of possible errors of the fluxes is difficult. No data are available to directly compare with; similar simulations have only been done with a less accurate and validated model (Le Hir et al., 2001) and measuring sediment fluxes (i.e., velocities and concentrations) with sufficiently high temporal and spatial resolution through an entire cross-section rather than only in a few water columns is close to impossible (e.g., Perez et al., 2000). At this point, only the comparison of simulated and actual dredged masses as well as of simulated sediment budgets and observed bathymetric changes can indicate the correctness of the fluxes and related processes, variables, and parameters, in addition to the traditional validation by comparison of simulated and measured water levels, velocities, and sediment concentrations. Both traditional validation and comparison of dredging were made in Part 1 (Grasso et al., 2018, section 3) and proved the model to satisfactorily reproduce those quantities.

The representativeness of simulated sediment fluxes in the lower estuary is further assessed by comparing simulated sediment budgets (resulting from fluxes and dredging/dumping) in experiments A–D to observed sediment budgets derived from bathymetric surveys conducted by the GPMR in the lower estuary from 2006 to 2014 (Table 4; Artelia, personal communication, November 2016; Artelia, 2014). The surveys covered the bathymetry below mean water level in the lower estuary approximately from the mouth to the Tancarville cross-section, but excluded the GPMH area (see Figure 2b). The surveys were carried out every year and required 6 months to be completed, yielding large bathymetric uncertainties of ± 10 cm, which corresponds to approximately $\pm 10 \times 10^6$ m³ over the entire area. The sediment budgets derived from the observed bathymetric changes range from -3 (loss) to 15×10^6 m³ (gain) per year with a long-term gain over the period 2006–2014, composed of balance during dry and moderate years (e.g., 2009–2012) and large gain during wet years (e.g., 2008 and 2013; Table 4). Note that these budgets are of the same order of magnitude as the measurement uncertainties; therefore, they can provide only a rough estimate of the sediment budgets observed in the lower estuary.

Table 4
Simulated Mass and Volume Budget of Total Sediment (Black Numbers) and Mud Fraction (Brown Numbers) in Experiments A–D Over One Lunar Year as Well as Observed Volume Budget of Total Sediment[a]

Exp.	Simulated mass and volume budget		Year	Observed volume budget and Q	
	Mass (10^7 kg)			(10^6 m^3)	(m^3/s)
A	216	−50	2006	6	418
B	182	−87	2007	7	485
C	587	251	2008	10	525
D	5	−131	2009	1	352
	Volume (10^6 m^3)		2010	0	414
A	0.86	−0.80	2011	−3	365
B	0.29	−1.39	2012	1	457
C	6.11	4.02	2013	15	717
D	−1.26	−2.10	2014	3	497

[a]Budgets from estuary mouth to Tancarville (mou, Tan in Figure 4a) excluding Le Havre harbor and access as well as areas above mean water level (see Figure 2b); positive for gain, negative for loss. Uncertainty of observations about $\pm 10 \times 10^6$ m^3. Q the average river discharge (cp. Figure 1m).

For comparison with the observations, sediment mass budgets (7) were calculated for the corresponding area (caption Table 4). These budgets directly result from the simulated fluxes and GPMR dredging activities. The simulated sediment mass budgets were transformed to volume budgets applying the deposit concentrations defined in Table 1.

The simulated sediment volume budgets in experiments A–D range from −2.1 to 6.1 × 10^6 m^3, mainly associated with loss of mud and gain of sand (exps. A, B, D; Table 4). However, in contrast to total sediment gain in experiments A and B (0.86 and 0.29 × 10^6 m^3, respectively), the large mud export during the stormy simulation (exp. D) results in total sediment loss (–1.26 × 10^6 m^3) as wave-induced sediment resuspension on the banks close to the estuary mouth may enhance seaward sediment fluxes. The high-discharge experiment C stands out with large sediment gain in the lower estuary (6.11 × 10^6 m^3) mainly due to large gain of mud opposing the loss of mud in experiments A, B, and D. This probably results from the ETM being located close to the estuary mouth and the strong baroclinic circulation due to high river discharge (Figure 9d versus 9c) reducing sediment export.

Due to the large measurement uncertainties, a validation of the simulated budget is not possible. However, the trends in relation to the forcing, which this study focused on, are comparable: Large sediment gain as in experiment C was also observed in 2013 ((15 ± 10) × 10^6 m^3), when the river discharge was particularly high (also see Figure 1m); sediment loss as in experiment D was also observed in 2011 ((–3 ± 10) × 10^6 m^3), when strong storms prevailed throughout December (see Figure 3c). Overall, the simulations covering typical and extreme forcing of the last 20 years fall in the range of the observed sediment budgets of the last 9 years, strengthening the confidence in the model representativeness.

4. Conclusions

By means of a thoroughly calibrated and validated high-resolution three-dimensional hydro- and sediment-dynamic model driven by realistic forcing, the mud and sand fluxes and budgets in the lower Seine Estuary could be quantified and investigated on seasonal to annual time scales. Hydro- and meteorological conditions affect the sediment fluxes and budgets in different ways and at different locations along the estuary:

1. Waves induce erosion offshore of the estuary mouth, particularly on the shallow banks; the wind direction determines the direction of the sediment fluxes offshore.
2. Estuarine circulation and tidal pumping generate up-estuary fluxes at the mouth and upstream cross-sections; spring tides cause significant up-estuary fluxes at the mouth cross-section.
3. A higher river discharge drives baroclinic up-estuary fluxes at (parts of) the downstream cross-sections and barotropic down-estuary fluxes at the upstream cross-sections.

This spatial pattern of the (relative) impact of wind and waves, tides, and river discharge along the Seine Estuary is in agreement with the description of the Columbia River Estuary (Sherwood & Creager, 1990, Figure 36) and it probably applies to the sediment fluxes in many other estuaries with similar characteristics. According to the location range of the Seine Estuary in the estuarine parameter space (section 1.3), examples of hydrodynamically similar systems are the strongly stratified Chesapeake Bay and Hudson River, the partially mixed James River and San Francisco Bay, the SIPS-regime Tamar River, and Conwy River as well as, consistent with the abovementioned agreement, the SIPS/salt-wedge Columbia River (Geyer & MacCready, 2014, Figure 6).

It should be noted again that, counterintuitively when having the barotropic effect of rivers in mind, a higher river discharge drives up-estuary sediment fluxes at certain downstream borders (channel entrance and offshore). This is a baroclinic effect caused by the (barotropic) down-estuary shift of the salt wedge and the associated increased horizontal salinity gradients and estuarine circulation at these deeper locations. Consequently, the lower estuary is substantially accretive during the wet year (6.11×10^6 m^3) compared to the slightly accretive reference year (0.86×10^6 m^3). Contrastingly, the stormy year is associated with sediment loss (-1.26×10^6 m^3).

While the model has been quantitatively validated with respect to water levels, salinities, wave heights, and velocities, sediment concentrations, and dredged masses (Part 1: Grasso et al., 2018, section 3), comparison of sediment budgets was only qualitatively possible due to the large uncertainties of the bathymetric surveys. However, these validations and comparisons as well as the only minor differences between simulations with different maximum settling velocities of mud provide confidence in the simulated sediment fluxes and budgets.

The environmental variables (such as current velocity, bed shear stress, salinity, and turbidity) which can be derived from these simulations represent a rich data set for ecological analyses of the Seine Estuary. Additionally, this study thoroughly investigating estuarine sediment dynamics under typical dry/wet and calm/stormy conditions provides interesting patterns which may be observed in other estuaries dominated by turbidity maximum dynamics.

References

Allen, G. P., Salomon, J. C., Bassoullet, P., Du Penhoat, Y., & de Grandpré, C. (1980). Effects of tides on mixing and suspended sediment transport in macrotidal estuaries. *Sedimentary Geology*, *26*(1), 69–90. https://doi.org/10.1016/0037-0738(80)90006-8

Amoudry, L. O., Ramirez-Mendoza, R., Souza, A. J., & Brown, J. M. (2014). Modelling-based assessment of suspended sediment dynamics in a hypertidal estuarine channel. *Ocean Dynamics*, *64*(5), 707–722. https://doi.org/10.1007/s10236-014-0695-8

Arakawa, A., & Lamb, V. R. (1977). Computational design of the basic dynamical processes of the UCLA general circulation model. In J. Chang (Ed.), *Methods in computational physics: Advances in research and applications, general circulation models of the atmosphere* (Vol. 17, pp. 173–265). Cambridge, MA: Academic Press.

Ardhuin, F., & Roland, A. (2012). Coastal wave reflection, directional spread, and seismoacoustic noise sources. *Journal of Geophysical Research: Oceans*, *117*, C00J20. https://doi.org/10.1029/2011JC007832

Artelia (2014). *Réhabilitation des vasières de l'estuaire de la Seine: Développement et exploitation d'un modèle hydrosédimentaire 3D de l'estuaire, analyse de l'évolution tendancielle* (Rapport 171 3203 R3, établi pour le compte du Grand Port Maritime du Havre en décembre). Lyon, France: Artelia.

Avoine, J., Allen, G. P., Nichols, M., Salomon, J. C., & Larsonneur, C. (1981). Suspended-sediment transport in the Seine estuary, France: Effect of man-made modifications on estuary-shelf sedimentology. *Marine Geology*, *40*(1–2), 119–137. https://doi.org/10.1016/0025-3227(81)90046-3

Bi, Q., & Toorman, E. A. (2015). Mixed-sediment transport modelling in Scheldt estuary with a physics-based bottom friction law. *Ocean Dynamics*, *65*(4), 555–587. https://doi.org/10.1007/s10236-015-0816-z

Bolle, A., Wang, Z. B., Amos, C., & De Ronde, J. (2010). The influence of changes in tidal asymmetry on residual sediment transport in the Western Scheldt. *Continental Shelf Research*, *30*(8), 871–882. https://doi.org/10.1016/j.csr.2010.03.001

Brenon, I., & Le Hir, P. (1998). Modelling fine sediment dynamics in the Seine estuary: Interaction between turbidity patterns and sediment balance. In J. Dronkers & M. Scheffers (Eds.), *Physics of estuaries and coastal seas* (pp. 103–114). Rotterdam, the Netherlands: A. A. Balkema.

Brenon, I., & Le Hir, P. (1999). Modelling the turbidity maximum in the Seine estuary (France): Identification of formation processes. *Estuarine, Coastal and Shelf Science*, *49*(4), 525–544. https://doi.org/10.1006/ecss.1999.0514

Burchard, H., & Baumert, H. (1998). The Formation of estuarine turbidity maxima due to density effects in the Salt Wedge. A hydrodynamic process study. *Journal of Physical Oceanography*, *28*(2), 309–321. https://doi.org/10.1175/1520-0485(1998)028<0309:TFOETM>2.0.CO;2

Burchard, H., Hetland, R. D., Schulz, E., & Schuttelaars, H. M. (2011). Drivers of residual estuarine circulation in tidally energetic estuaries: Straight and irrotational channels with parabolic cross section. *Journal of Physical Oceanography*, *41*, 548–570. https://doi.org/10.1175/2010JPO4453.1

Burchard, H., Schuttelaars, H. M., & Geyer, W. R. (2013). Residual sediment fluxes in weakly-to-periodically stratified estuaries and tidal inlets. *Journal of Physical Oceanography*, *43*(9), 1841–1861. https://doi.org/10.1175/JPO-D-12-0231.1

Cancino, L., & Neves, R. (1999). Hydrodynamic and sediment suspension modelling in estuarine systems: Part II: Application to the Western Scheldt and Gironde estuaries. *Journal of Marine Systems*, *22*(2–3), 117–131. https://doi.org/10.1016/S0924-7963(99)00036-6

Deloffre, J., Verney, R., Lafite, R., Lesueur, P., Lesourd, S., & Cundy, A. B. (2007). Sedimentation on intertidal mudflats in the lower part of macrotidal estuaries: Sedimentation rhythms and their preservation. *Marine Geology*, *241*(1–4), 19–32. https://doi.org/10.1016/j.margeo.2007.02.011

Dronkers, J. (1986). Tide-induced residual transport of fine sediment. In J. van de Kreeke (Ed.), *Physics of shallow estuaries and bays* (pp. 228–244). New York, NY: Springer-Verlag. https://doi.org/10.1029/LN016p0228

Dyer, K. R. (1973). *Estuaries: A physical introduction* (140 p.). London, UK: John Wiley & Sons.

Festa, J. F., & Hansen, D. V. (1976). A two-dimensional numerical model of estuarine circulation: The effects of altering depth and river discharge. *Estuarine, Coastal and Marine Science*, *4*(3), 309–323. https://doi.org/10.1016/0302-3524(76)90063-3

Festa, J. F., & Hansen, D. V. (1978). Turbidity maxima in partially mixed estuaries: A two-dimensional numerical model. *Estuarine, Coastal and Marine Science*, *7*(4), 347–359. https://doi.org/10.1016/0302-3524(78)90087-7

French, J. R., Burningham, H., & Benson, T. (2008). Tidal and meteorological forcing of suspended sediment flux in a muddy mesotidal estuary. *Estuaries and Coasts*, *31*(5), 843–859. https://doi.org/10.1007/s12237-008-9072-5

Garel, E., Pinto, L., Santos, A., & Ferreira, O. (2009). Tidal and river discharge forcing upon water and sediment circulation at a rock-bound estuary (Guadiana estuary, Portugal). *Estuarine, Coastal and Shelf Science*, *84*(2), 269–281. https://doi.org/10.1016/j.ecss.2009.07.002

Geyer, W. R. (1993). The importance of suppression of turbulence by stratification on the estuarine turbidity maximum. *Estuaries*, *16*(1), 113–125. https://doi.org/10.2307/1352769

Geyer, W. R., & MacCready, P. (2014). The estuarine circulation. *Annual Review of Fluid Mechanics*, *46*, 175–197. https://doi.org/10.1146/annurev-fluid-010313-141302

Gibson, R. E., England, G. L., & Hussey, M. J. L. (1967). The theory of one-dimensional consolidation of saturated clays. *Géotechnique*, *17*(3), 261–273. https://doi.org/10.1680/geot.1967.17.3.261

Gleizon, P., Punt, A. G., & Lyons, M. G. (2003). Modelling hydrodynamics and sediment flux within a macrotidal estuary: problems and solutions. *Science of the Total Environment*, *314–316*, 589–597. https://doi.org/10.1016/S0048-9697(03)00075-5

Grasso, F., Le Hir, P., & Bassoullet, P. (2015). Numerical modelling of mixed-sediment consolidation. *Ocean Dynamics*, *65*(4), 607–616. https://doi.org/10.1007/s10236-015-0818-x

Grasso, F., Verney, R., Le Hir, P., Thouvenin, L., Schulz, B., Kervella, E., . . . Garnier, V. (2018). Suspended sediment dynamics in the macrotidal Seine Estuary (France): 1. Numerical modeling of turbidity maximum dynamics. *Journal of Geophysical Research: Oceans*, *123*, https://doi.org/10.1002/2017JC013185

Hansen, D. V., & Rattray, M. Jr. (1965). Gravitational circulation in straits and estuaries. *Journal of Marine Research*, *23*, 104–122.

Jalón-Rojas, I., Schmidt, S., Sottolichio, A., & Bertier, C. (2016). Tracking the turbidity maximum zone in the Loire Estuary (France) based on a long-term, high-resolution and high-frequency monitoring network. *Continental Shelf Research*, *117*, 1–11. https://doi.org/10.1016/j.csr.2016.01.017

Jay, D. A., & Musiak, J. D. (1994). Particle trapping in estuarine tidal flows. *Journal of Geophysical Research: Oceans*, *99*, 20445–20461. https://doi.org/10.1029/94JC00971

Kervella, Y., Khojasteh Pour Fard, I., Le Hir, P., Renault, E., & Lemoine, J.-P. (2012). Modélisation hydrodynamique tridimensionelle en coordonnées curvilignes non-orthogonales de l'estuaire de la Seine. *XIIèmes Journées Nationales Génie Côtier - Génier Civil, Revue Paralia*, *5*, 89–100. https://doi.org/10.5150/jngcgc.2012.010-K

Lambrechts, J., Humphrey, C., McKinna, L., Gourge, O., Fabricius, K. E., Mehta, A. J., . . . Wolanski, E. (2010). Importance of wave-induced bed liquefaction in the fine sediment budget of Cleveland Bay, Great Barrier Reef. *Estuarine, Coastal and Shelf Science*, *89*(2), 154–162. https://doi.org/10.1016/j.ecss.2010.06.009

Lazure, P., & Dumas, F. (2008). An external-internal mode coupling for a 3D hydrodynamical model for applications at regional scale (MARS). *Advances in Water Resources*, *31*(2), 233–250. https://doi.org/10.1016/j.advwatres.2007.06.010

Le Hir, P., Cayocca, F., & Waeles, B. (2011). Dynamics of sand and mud mixtures: A multiprocess-based modelling strategy. *Continental Shelf Research*, *31*(10), S135–S149. https://doi.org/10.1016/j.csr.2010.12.009

Le Hir, P., Ficht, A., Jacinto, R. S., Lesueur, P., Dupont, J.-P., Lafite, R., . . . Cugier, P. (2001). Fine sediment transport and accumulations at the mouth of the Seine estuary (France). *Estuaries*, *24*(6), 950–963. https://doi.org/10.2307/1353009

Le Provost, C., Fornerino, M., & Villaret, C. (1986). Sur l'hydrodynamique de la baie de Seine. Résultats d'observations et de modélisations. In *La baie de Seine (GRECO-Manche)* (Vol. 4, pp. 43–48). Brest, France: IFREMER. http://archimer.ifremer.fr/doc/1985/acte-1259.pdf

Lerczak, J. A., & Geyer, W. R. (2004). Modeling the lateral circulation in straight, stratified estuaries. *Journal of Physical Oceanography*, *34*, 1410–1428. https://doi.org/10.1175/1520-0485(2004)034<1410:MTLCIS>2.0.CO;2

Lesourd, S., Lesueur, P., Fisson, C., & Dauvin, J.-C. (2016). Sediment evolution in the mouth of the Seine estuary (France): A long-term monitoring during the last 150 years. *Comptes Rendus Geoscience*, *348*, 442–450. https://doi.org/10.1016/j.crte.2015.08.001

Lindsay, P., Balls, P. W., & West, J. R. (1996). Influence of tidal range and river discharge on suspended particulate matter fluxes in the Forth Estuary (Scotland), *Estuarine, Coastal and Shelf Science*, *42*(1), 63–82. https://doi.org/10.1006/ecss.1996.0006

Lumborg, U. (2005). Modelling the deposition, erosion, and flux of cohesive sediment through Øresund. *Journal of Marine Systems*, *56*(1–2), 179–193. https://doi.org/10.1016/j.jmarsys.2004.11.003

Lumborg, U., & Pejrup, M. (2005). Modelling of cohesive sediment transport in a tidal lagoon: An annual budget. *Marine Geology*, *218*(1–4), 1–16. https://doi.org/10.1016/j.margeo.2005.03.015

Lumborg, U., & Windelin, A. (2003). Hydrography and cohesive sediment modelling: Application to the Rømø Dyb tidal area. *Journal of Marine Systems*, *38*(3–4), 287–303. https://doi.org/10.1016/S0924-7963(02)00247-6

Marmin, S., Dauvin, J.-C., & Lesueur, P. (2014). Collaborative approach for the management of harbour-dredged sediment in the Bay of Seine (France). *Ocean & Coastal Management*, *102*, 328–339. https://doi.org/10.1016/j.ocecoaman.2014.10.012

McSweeney, J. M., Chant, R. J., & Sommerfield, C. K. (2016). Lateral variability of sediment transport in the Delaware Estuary. *Journal of Geophysical Research: Oceans*, *121*, 725–744. https://doi.org/10.1002/2015JC010974

Nitsche, F. O., Kenna, T. C., & Haberman, M. (2010). Quantifying 20th century deposition in complex estuarine environment: An example from the Hudson River. *Estuarine, Coastal and Shelf Science*, *89*(2), 163–174. https://doi.org/10.1016/j.ecss.2010.06.011

Partheniades, E. (1965). Erosion and deposition of cohesive soils. *Journal of the Hydraulics Division American Society of Civil Engineering*, *91*(1), 105–139.

Perez, B. C., Day, J. W. Jr, Rouse, L. J., Shaw, R. F., & Wang, M. (2000). Influence of Atchafalaya river discharge and winter frontal passage on suspended sediment concentration and flux in Fourleague Bay, Louisiana. *Estuarine, Coastal and Shelf Science*, *50*(2), 271–290. https://doi.org/10.1006/ecss.1999.0564

Ralston, D. K., Geyer, W. R., & Warner, J. C. (2012). Bathymetric controls on sediment transport in the Hudson River estuary: Lateral asymmetry and frontal trapping. *Journal of Geophysical Research: Oceans*, *117*, C10013. https://doi.org/10.1029/2012JC008124

Schulz, E., Schuttelaars, H. M., Gräwe, U., & Burchard, H. (2015). Impact of the depth-to-width ratio of periodically stratified tidal channels on the estuarine circulation. *Journal of Physical Oceanography*, *45*(8), 2048–2069. https://doi.org/10.1175/JPO-D-14-0084.1

Scully, M. E., & Friedrichs, C. T. (2007). Sediment pumping by tidal asymmetry in a partially mixed estuary. *Journal of Geophysical Research*, *112*, C07028. https://doi.org/10.1029/2006JC003784

Sherwood, C. R., & Creager, J. S. (1990). Sedimentary geology of the Columbia river estuary. *Progress in Oceanography*, *25*(1), 15–79. https://doi.org/10.1016/0079-6611(90)90003-K

Sommerfield, C. K., & Wong, K.-C. (2011). Mechanisms of sediment flux and turbidity maintenance in the Delaware Estuary. *Journal of Geophysical Research*, *116*, C01005. https://doi.org/10.1029/2010JC006462

Soulsby, R. (1997). *Dynamics of marine sands: A manual for practical applications* (249 p.). London, UK: Thomas Telford.

Talke, S. A., & Stacey, M. T. (2008). Suspended sediment fluxes at an intertidal flat: The shifting influence of wave, wind, tidal, and freshwater forcing. *Continental Shelf Research*, *28*(6), 710–725. https://doi.org/10.1016/j.csr.2007.12.003

Thouvenin, B., Gonzalez, J. L., Chiffoleau, J. F., Boutier, B., & Le Hir, P. (2007). Modelling Pb and Cd dynamics in the Seine estuary. *Hydrobiologia*, *588*(1), 109–124. https://doi.org/10.1007/s10750-007-0656-z

Toublanc, F., Brenon, I., & Coulombier, T. (2016). Formation and structure of the turbidity maximum in the macrotidal Charente estuary (France): Influence of fluvial and tidal forcing. *Estuarine, Coastal and Shelf Science*, *169*, 1–14. https://doi.org/10.1016/j.ecss.2015.11.019

Uncles, R. J., Elliott, R. C. A., & Weston, S. A. (1985). Observed fluxes of water, salt and suspended sediment in a partly mixed estuary. *Estuarine, Coastal and Shelf Science*, *20*(2), 147–167. https://doi.org/10.1016/0272-7714(85)90035-6

Uncles, R. J., Stephens, J. A., & Barton, M. L. (1992). Observations of fine-sediment concentrations and transport in the turbidity maximum region of an estuary. In D. Prandle (Ed.), *Dynamics and exchanges in estuaries and the coastal zone* (pp. 255–276). Washington, DC: American Geophysical Union. https://doi.org/10.1029/CE040p0255

van Leussen, W. (1994). *Estuarine macroflocs and their role in fine-grained sediment transport* (PhD thesis). Utrecht, the Netherlands: University of Utrecht.

Verney, R., Deloffre, J., Brun-Cottan, J.-C., & Lafite, R. (2007). The effect of wave-induced turbulence on intertidal mudflats: Impact of boat traffic and wind. *Continental Shelf Research*, *27*(5), 594–612. https://doi.org/10.1016/j.csr.2006.10.005

Yarbro, L. A., Carlson, P. R., Fisher, T. R., Chanton, J. P., & Kemp, W. M. (1983). A sediment budget for the Choptank River estuary in Maryland, U.S.A. *Estuarine, Coastal and Shelf Science*, *17*(5), 555–570. https://doi.org/10.1016/0272-7714(83)90007-0

Yu, Q., Wang, Y., Gao, J., Gao, S., & Flemming, B. (2014). Turbidity maximum formation in a well-mixed macrotidal estuary: The role of tidal pumping. *Journal of Geophysical Research: Oceans*, *119*, 7705–7724. https://doi.org/10.1002/2014JC010228